Graphene Loading Induced Effects on Characteristics of $Fe_xW_{1-x}O_3$ Nanostructures

By

Abdul Qadir

Supervised by

Dr. Javed Iqbal Saggu

Laboratory of Nanoscience and Technology (LNT)

Department of Physics

Quaid-i-Azam University

Islamabad, Pakistan

2018

This work is submitted as a dissertation in partial fulfillment of the requirement for the degree of

MASTER OF PHILOSOPHY

IN

PHYSICS

To

Department of Physics

Quaid-i-Azam University

Islamabad, Pakistan

2018

Certificate

This is to certify that the thesis entitled **"Graphene Loading Induced Effects on Characteristics of $Fe_xW_{1-x}O_3$ Nanostructures"** by **Mr. Abdul Qadir,** submitted to Quaid-i-Azam University, Islamabad, for the degree of Master of Philosophy in Physics is a record of bonafide research work carried out by him in the Laboratory of Nanoscience and Technology (LNT), Department of Physics under my supervision. I believe that this thesis fulfills the part of requirement for the award of Master of Philosophy.

Supervisor	**Head of Department**
Dr. Javed Iqbal Saggu	**Prof. Dr. Arif Mumtaz**
Associate Professor	Chairman
Department of Physics	Department of Physics
Quaid-i-Azam University	Quaid-i-Azam University
Islamabad, Pakistan.	Islamabad, Pakistan.

Declaration

I, Abdul Qadir, hereby declare that this project **"Graphene Loading Induced Effects on Characteristics of $Fe_xW_{1-x}O_3$ Nanostructures"** submitted by me under the guidance and supervision of Dr. Javed Iqbal Saggu Associate Professor at Quaid-i-Azam university, Islamabad is my own work and has not been submitted to any other university, institute or published earlier. The plagiarism test has been carried out using Turnitin Software via ID: 1003859423 and lies in permissible range (8% similarity index). However, at any stage, if this work is found to be plagiarized, I only (Abdul Qadir) myself will be held responsible for it as per rules and regulations.

_____

Abdul Qadir

Dedicated

to

My parents (Deceased), brothers and sisters.

They are always a source of strength, encouragement and inspiration for me.

Acknowledgment

Foremost, I would like to pay my deepest gratitude to Almighty **ALLAH**, who blessed me with motivation and strength for completing my research. Next, I offer my earnest gratefulness to the **Holy Prophet (Peace be Upon Him)** who is a source of guidance and knowledge for humanity.

My special and heartily thanks to my supervisor, **Dr. Javed Iqbal Saggu** who encouraged and directed me. His challenges brought this work towards a completion. It is with his supervision that this work came into existence. His enthusiasm and devotion to work has been an inspiration for me and I appreciate all his guidance and support during my work with him.

I am grateful to my research fellows Ghulam Muhauddin and Sadia Ehsan for academic support and friendship. I am also grateful to my seniors Muhammad Saleem, Sohail Azmat, Muhammad Israr, Sobia Jabeen and Hamsa Noreen at LNT QAU, Islamabad, for showing confidence in my work and for their patience and help.

A special word of gratitude is due to Faisal Mehmood, Kashif Ali and Waheed, all of whom never stopped challenging me and helping me develop my ideas. I must also express my gratitude to my juniors at LNT, Syed Umair Hamid, Maria Rani and Misbah Rani for providing a fun filled and stimulating environment.

Nobody has been more important to me in the pursuit of this thesis than the members of my family. I would like to thank my brothers and sisters; whose love, guidance is with me and prayed for me throughout the time of my research. They are the ultimate role models.

Abdul Qadir

Abstract

The $Fe_xW_{1-x}O_3$ {x= 0, 3, 5, 7 & 10} nanoparticles have been synthesized using facile chemical co-precipitation process and by *ex-situ* method, nanocomposites of $(Fe_xW_{1-x}O_3)_{0.5}(GNPs)_{0.5}$ {x= 0, 3, 5, 7 & 10} have also been prepared. The structural, morphological, vibrational and optical properties have been investigated via XRD, SEM, FTIR and DRS analysis respectively. The XRD patterns confirm the formation of both phases; WO_3 and graphene nanoplatelets (GNPs), coexisting together without any impurity phase of dopant in WO_3. The SEM images depict the spherical particle like morphology of pristine WO_3 and $Fe_xW_{1-x}O_3$ nanoparticles while GNPs show plates like morphology. The WO_3 nanoparticles seem to be embedded in GNPs, which is observed by SEM images. FTIR, investigations demonstrate the stretching vibration mode of W-O-W and ruled out the formation of extra phase of Fe-O vibration mode. The optical band gap of tungsten trioxide has been modified upon Fe doping that is ascribed to shift in the valence band. The incorporation of 50% GNPs with $Fe_xW_{1-x}O_3$ nanoparticles enhanced ultraviolet light driven photocatalytic degradation of methyl blue, which is attributed to charge trapped in crystal defects. Furthermore, the appropriate quantity of GNPs in $(Fe_xW_{1-x}O_3)_{0.5}(GNPs)_{0.5}$ {x= 0, 3, 5, 7 & 10} nanocomposite, renders it as an exceptional antibacterial material with 80% growth inhibition of both the *Staphylococcus epidermidis* (Gram-positive bacteria) and *Klebsiella pneumoniae* (Gram-negative bacteria). Hence, this novel nanocomposite can be used to achieve efficient pathogen control along with economic photocatalyst for solution of waste water treatment.

Table of Contents

List of Figures

List of Tables

Chapter No.1

Introduction

1.1 Materials Science

The word material is a broad term normally used for a substance or its mixture. In the sense of metaphysics, material can be anything consisting of whether non-living, impure abstract, man-made, living, pure, concrete or natural matter. Materials can be defined as; an inanimate solid used by an engineer in the practice of his profession. In material engineering, different properties and applications of materials are studied. It is an integrative field concerning the study of applications and kinds of materials to several fields of engineering and science. It associates elements of the applied Physics and Chemistry along with other engineering branches like civil, mechanical, chemical and electrical engineering. Among the different types of materials, graphene and their composites are commonly used for various kinds of applications in human life. These composites play vital role in Material Science and Technology because their physical and chemical properties can be tuned by increasing or decreasing the weight percent of host materials for required application.

1.2 Nanomaterials and their Applications

The recent research in the field of Material Science is mainly focus on nanomaterials. The main importance of this field is to differentiate these new materials from their bulk and prepare these nanomaterials for the use of human life in future [1-5]. The study of nanomaterials is known as nanoscience. To discover new physical properties and understand possible applications of nanomaterials, the capability to construct and develop nanostructures is the

primary foundation stone in nanoscience and technology. Due to the technological importance and its unique properties this new science has become the attention of materials scientists [6-10].

Nanoparticle can be defined as; a particle whose at least one dimension is in nanometer range. Due to the difference in size, one can differentiate these nanomaterials from their bulk. At nanoscale, nanomaterials show unique properties [11-17]. These unique properties occur due to two prominent effects; surface atoms to volume ratio and quantum confinement effect. The ratio for the surface atoms to volume of nanomaterials is large as compare to the bulk materials, which results it unique properties. The morphology of nanomaterials also depends on their properties and can be shaped as nanospheres, nanowires, nanotubes, nanorods, nanoplates and nanocubes using different synthesis techniques. Depending on the improved characteristics of the nanomaterials as compared to the bulk, numerous high value applications have been anticipated [18-30]. The nanomaterials and their composite are being used in data storage devices, nano-sensors, solar cells, targeted drug delivery, water purification and photocatalysis [31-34].

1.2.1 Nanomaterials Classifications

Materials for which at least one of the external dimensions is in nanometer range are termed as nanomaterials. These nanomaterials are further classified into three groups according to their confined dimensions. In zero-dimension nanomaterials, all the three dimensions are limited to nanoscale. In case of one dimensional nanomaterials, two out of three dimensions are limited to nanoscale and in two dimensional nanomaterials, one dimension out of three dimensions is limited to nanoscale. The schematic diagram for zero, one and two-dimensional nanomaterials has been shown in figure 1.1. In zero-dimensional nanomaterials, all the three dimensions occur in the range of nanoscale. None of the dimension occur at the bulk level [35]. For example, nanoparticles and quantum dots.

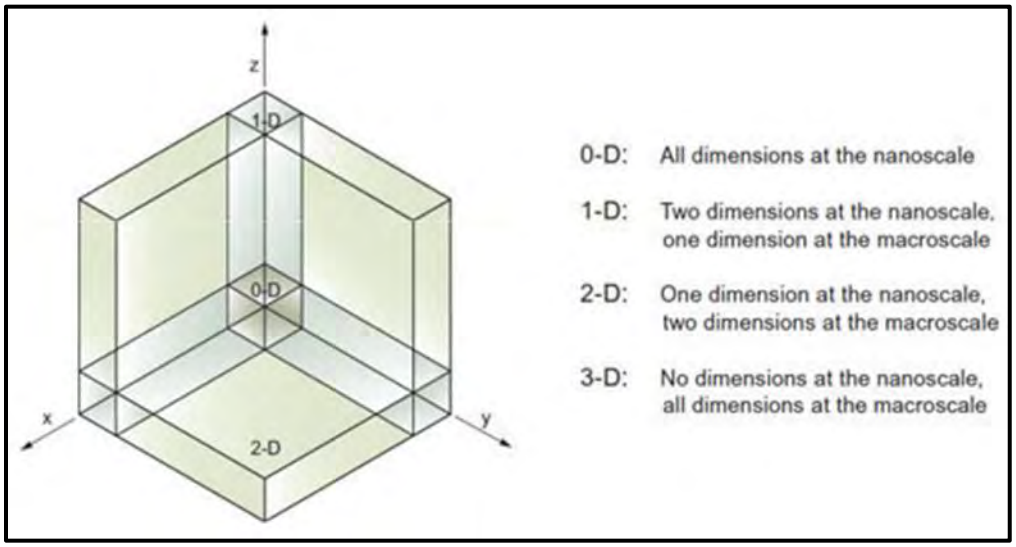

Figure 1.1 Classification of nanoscale dimensions.

One-dimensional nanomaterials are those whose one dimension is in the bulk while two dimensions are at the nanoscale. e.g. nanowires and nanorods etc. Nanomaterials for which two dimensions are at the bulk and one of its dimension is confined to nanoscale are termed as two-dimensional nanomaterials. i.e. nanoplates and nanofilms etc. Materials for which all the three dimensions are at macroscale are termed as bulk materials.

1.3 Physical Properties of Nanomaterials

The physical properties of the nanomaterials as compared to their bulk counterpart show tremendous change because of the atomic scale dimension of the nanomaterials. Among those odd properties some of them has already been recognized while others need to be exposed yet. Literature reveals that reduced imperfections, spatial confinement, large value for surface energy and large portion of surface atoms are the major roots for the odd physical properties of nanomaterials [36]. In short, we can say that material properties are size dependent. These properties can further divide into four types;

1.3.1 Optical Properties

In comparison, the optical properties for nanomaterials could be dramatically changed as compare with the bulk materials of the same nature. i.e. For a semiconductor nanomaterial, the absorbance maximum moves toward the lower wavelength because of the high value for band gap. Surface plasmon resonance also alters the color for nanoparticles in various metals due to the variation in their sizes.

Generally, the nanomaterials show peculiar optical properties because of the interaction of light with their nanostructure. The color properties of nanomaterials are very different for the same materials at their bulk form. The reason behind this is the interaction of light with materials. When light interacts with matter, certain wavelengths absorb by materials are not seen by an observer. On the other hand, an observer sees the light, only reflected from the materials, which give material a specific color. For example, leaves seem to be green because of the chlorophyll that absorb the red and blue colors and reflect the green.

Normally there are three phenomenon occurs when light is incident on a material.

$$I = R + A + T \tag{1.1}$$

Where R, A and T refer to reflection, absorption and transmittance. Scattering of light also play an important role in materials color especially at nanoscale. No change in the reflected and incident wave will occur when light hit a material surface and reflects in the same medium. Molecular phenomenon strongly dependent on the structure of the substance and its chemical identity involves energy transformation, electronic transitions, rotations and vibrations is known as absorption. Wavelength of the absorbed light can be determined by the energy levels of that material. The fraction of the intensity of the transmitted light to the intensity of the incident light

is called transmittance while the process in which photons strike the surface of materials whose size is nearly equal with the wavelength of incoming light is called scattering. The wavelength remains same for the outgoing and incoming light. Scattering is a phenomenon which is strongly linked with index of refraction of the medium, refractive index of cluster as well as the size of the cluster. Energy transformation not occur in this physical process. For maximum scattering, the wavelength of the light must be double as the size of the cluster. For example, if the size of the bunch is 250 nm, the maximum value of its scattering will be 500 nm, that confirms it is in the visible range [37].

Semiconductors in nanosized have discrete energy levels due to quantum confinement effect from which energy once absorbed by the materials can be emitted. This phenomenon is known as quantum fluorescence. For example, semiconductor quantum dots. The valence and conduction bands split and become quantized in semiconductor materials at its nanoform. When transformation of charge occurs at these levels, certain dimension of wavelengths is absorbed that result monochromatic emission. Since quantum confinement effect increases the energy of bandgap. Therefore, for a semiconducting material, a large amount of energy is required for the bandgap during absorption. Large amount of energy means that wavelength decreases, and this phenomenon is termed a blue shift. For semiconducting materials, the size should be tune first before tuning its bandgap. This is the reason that the same materials emit different colors at different size [38].

1.3.1.1 Optical Band Gap

Materials whose conductivity lies between conductors and insulators are known as semiconductors. They may be natural as well as artificial. The minimum difference in energy at

the valence band maxima and conduction band minima is called band gap. Each semiconductor material has its own band gap energy.

During quantum confinement and doping, only the physical properties of the material changes while the chemical properties remain the same. Based on band gap, semiconductors have been divided into two categories;

1.3.1.2 Direct Band Gap Semiconductors

The type of semiconductor materials in which minima of the conduction and maxima of the valence band are at the same value of electron momentum are known as direct band gap semiconductors. It is due to this reason, when a photon of energy greater or equal to the band gap incident on such type of semiconductor materials produces electron-hole pair very easily. For example, Zinc oxide (ZnO), ZnSe and Gallium Arsenide (GaAs) are direct band gap semiconductor [39]. Absorption spectroscopy is the simplest method to determine the band gap by plotting photon energy at x-axis and coefficient of absorption on y-axis [40]. To determine the band gap for direct band gap semiconductors, the light frequency and the coefficient of absorption linked by the following relation;

$$\alpha = \boldsymbol{A}^* \sqrt{h\vartheta - E_g} \tag{1.2}$$

with

$$A^* = \frac{q^2 x_{\vartheta c}^2 (2m_\tau)^{\frac{3}{2}}}{\lambda_0 \epsilon_0 \hbar^3 n} \tag{1.3}$$

In the above formula α, h, E_g, υ, q, $x_{\upsilon c}$, A^*, $\hbar$, ϵ_0 and n represent absorption coefficient, Planck's constant, energy of band gap, frequency of light, elementary charge, matrix element like the lattice constant, certain frequency, reduced Planck's constant, permittivity of free space, index of refraction and m_τ is called reduced mass which can be calculated using equation;

$$m_\tau = \frac{m_h^* m_e^*}{m_h^* + m_e^*} \tag{1.4}$$

Where m_h^* and m_e^* denotes the hole and electron effective masses. This formula is valid for light with larger photon energy [41].

1.3.1.3 Indirect Band Gap Semiconductors

In this class of semiconductor materials, the minima of the conduction and maxima of the valence band are not at the same value of electron's momentum. Therefore, it is very difficult to produce electron-hole pair when a photon of any energy incident on such materials. Indirect band gap material includes Germanium and Silicon. The formula for the determination of indirect band gap is

$$\alpha \propto \frac{\left(h\vartheta - E_g - E_p\right)^2}{e^{\left(\frac{E_p}{KT}\right)} - 1} + \frac{\left(h\vartheta - E_g - E_p\right)^2}{1 - e^{\left(-\frac{E_p}{KT}\right)}} \tag{1.5}$$

Where T and K is the temperature and Boltzmann's constant and E_g represents phonon energy. By plotting photon energy versus square of the absorption coefficient, a tangent line is extended toward x-axis, the intersection points at which α = 0 is the corresponding value of the band gap. The calculated value will be the band gap for direct band gap semiconductor materials. In order to calculate the band gap for indirect semiconductor materials, the photon energy is plotted against square root of the absorption coefficient.

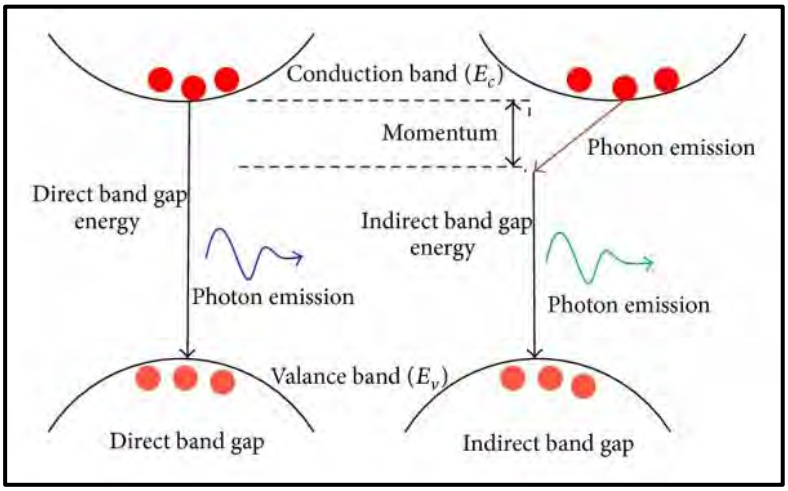

Figure 1.2 Direct and Indirect bandgaps.

Figure 1.2 Schematic diagram for direct and indirect band gap semiconductors.

1.3.1.4 Quantum Confinement Effect

By reducing the dimension or size of a material from macroscopic to lower scale, such as meter or centimeter, the physical properties of the materials remain the same, but when the size or dimension is decrease further, small changes occur at first, until when the size is reduced below 100 nm, dramatic changes in properties can occur [42]. This is due to quantum confinement. For semiconductor materials the quantum confinement effect plays a vital role especially when the size of the particle is comparable to the Bohr exciton radius. For a particle, Bohr radius can be calculated from the given equation;

$$a_B = \frac{m}{m^*}\varepsilon a_o \qquad (1.6)$$

Where α_B is the Bohr exciton radius, a_o represents the Bohr radius for hydrogen atom, m represents rest mass of an electron, m^* shows the particle mass and $\boldsymbol{\varepsilon}$ is the dielectric constant of the material.

The word confinement means to restrict the motion of electrons in discrete energy levels and quantum replicates the atomic realm of atoms. When the diameter of the particle becomes equal or same as the magnitude of the wavelength of the electron then quantum confinement effect can easily be observed.

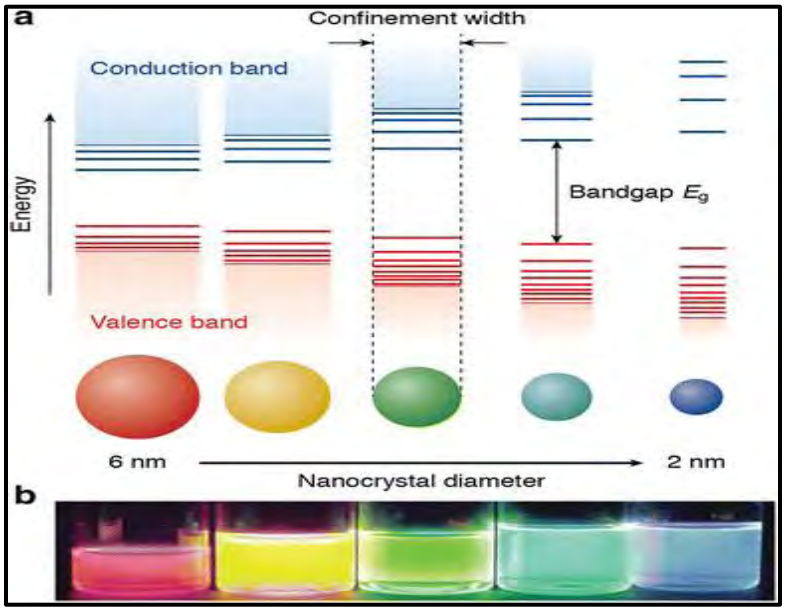

Figure 1.3 (a) Diagram shows that as the particle size decreases the band gap increases **(b)** Photographs demonstrate CdSe QDs colloidal dispersions with different sizes [43].

As we go from bulk materials to nanomaterials tremendous change occur in their optical and electronic properties. Also, when size of a particle reaches to nanoscale the decrease in confining dimension makes the energy levels discrete that increase the energy of the band gap. Hence, increase in the band gap of materials is due to quantum confinement effect. Figure 1.3 represents CdSe quantum dots that confirms the increase of the band gap with the decrease in the particle size.

1.3.1.5 Surface to Volume Ratio

The chemical and physical properties of the materials whether nanoscale or bulk depend strongly on the surface properties of these materials. Since surface accomplish several roles; as in case of catalyst surface can terminate or initiate a chemical reaction, permit energy flow or stream of materials at the boundary and keep things out and in. The structural properties like symmetry and lattice parameters are highly influenced by scaling down of bulk materials to nanoscale materials [44]. At nanoscale, various parameters in the lattice i.e. stress and surface energy are increased and cause thermodynamic instability. Due to this variability, physical modifications and lattice parameters occur. Nanomaterials possess structural stability by having minimum value for surface energy.

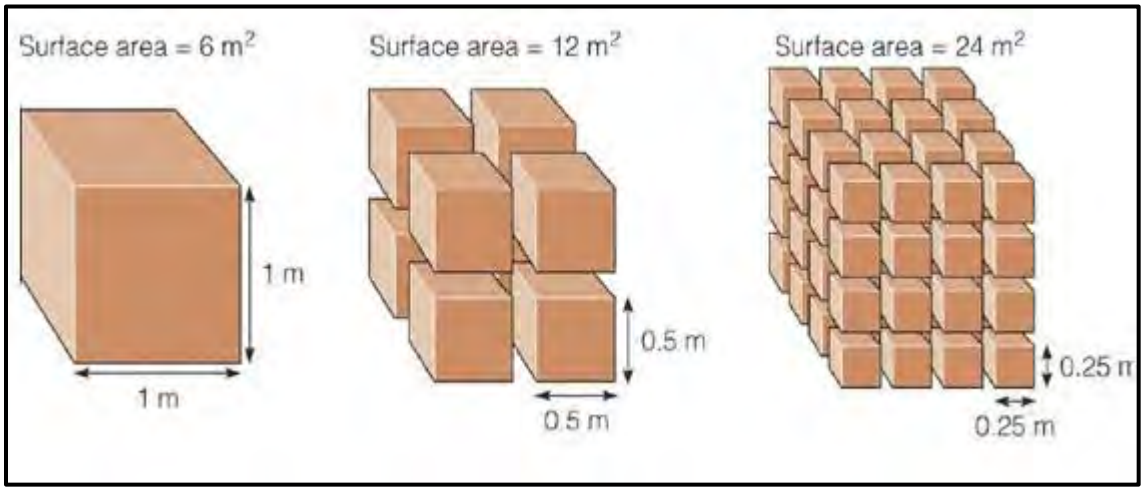

Figure 1.4 Schematic representation of surface to volume ratio[45].

Consider the difference between the bulk and nanocubes for a material as shown in figure 1.4. Total volume is similar for both the cubes, but the surface area is very greater for the nanocubes. As the particle size decreases, the surface area of the nanocubes is highly increased, because large number of atoms lodges on the surface. The high surface area makes the

nanomaterials chemically very reactive because more atoms has been exposed to the surface and can take part during reaction. Materials having small particle size will be more reactive as compared to the larger one. It means, that there is an inverse relation between chemical reactivity of a material and its particle size.

1.3.2 Magnetic Properties

Generally, the magnetic properties of the materials can be described by magnetization plot. For a ferromagnetic material, the magnetization curve is the graph between total magnetization M versus applied field with strength H as shown in figure 1.5. The applied field depends directly on magnetization. The magnetization goes on increasing when the magnitude of applied field is increased until a specific value known as a saturation point M_s. On the other hand, when the value of applied field is reduced from the saturation point, the value of magnetization goes on decreasing but not to the same value it had before, but as the field is low, curve show higher value, which is commonly known as hysteresis [46]. For a material, the magnetization that still exist after the removal of the applied field is termed as remnant magnetization M_r. To remove the remnant magnetization, one must apply the field H_c in the opposite direction to the field applied initially. Where H_c represents the coercive field.

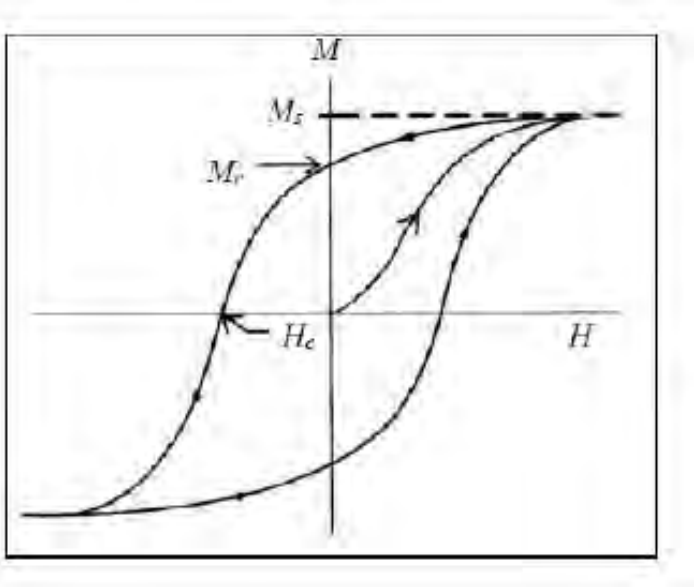

Figure 1.5 M-H loop of ferromagnetic material.

The magnetic properties of a material depend on the temperature as well as the structure of the material. For a material to have a magnetic property there must exist a nonzero net spin. As we know that size of the magnetic domain is 1μm classically, but when size of these magnetic domains is reduced to nanoscale, quantum effects start to dominate, and these materials show new properties. For example, one of these new properties; that is used in storage devices is GMR effect (Giant Magnetoresistance Effect).

1.3.3 Mechanical Properties

Nanomaterials show dramatic change in their mechanical properties for a single crystal as compare with its bulk counterpart. The reason behind this is the reduction in the probability of defects.

Related to the structure, some of the nanomaterials have exceptional mechanical properties. One of the best example is carbon nanotube, which may be multi-walled or single-walled lighter pipes that has structure like graphite but properties very different from the

graphite. In comparison, these pipes or tubes as shown in figure 1.6 are very lighter and hundred times stronger than steel. The primary method to enhance mechanical properties for a given material is to convert it into nanoscale. For this purpose, nanocomposites are formed. Nanomaterials show improved mechanical properties like hardness and toughness etc. In polycrystalline structures, defects e.g., dislocations or cracks are present [47]. When these crystalline materials are subjected to mechanical stress, fracture are produced. This is because of the defect that permit these dislocations to spread.

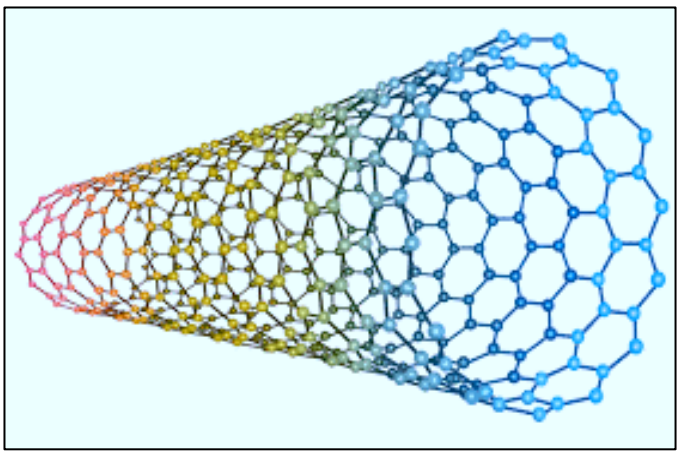

Figure 1.6 Carbon nanotube single walled Manifestation.

To block these dislocations and cracks, some other materials nanoparticles are added with lattice of the primary materials. This is the basic reason that these materials have high mechanical properties and used largely in coatings. Both organic and inorganic composites can be used for the improvement of mechanical properties using nanoparticles of different materials.

1.3.4 Electrical Properties

Electrical properties of nanomaterials not only depend upon the surface scattering, but these properties also depend on the arrangement of microstructure. By reducing the particle size, surface scattering enhances which results in the decrease in electrical conductivity for that

material. On the other hand, if the microstructures are arranged in better way like in polymeric fibrils then it increases the electrical conductivity for that materials [48].

Quantum effects are more prominent when one or more dimensions of semiconductor materials are reduced at nanoscale. These effects, especially the existence of discrete energy levels and the existence of a phenomenon known as quantum tunneling can be use in electrical properties. At nanoscale, the electrical properties of the material changes dramatically. Materials that are conductors in bulk form may become poor conductors or semiconductors at nanoscale. Some other materials that were semiconductors may become superconductors or conductors. The confinement of electrons at nanoscale change electrical properties of material.

1.4 Semiconducting Oxides

Semiconducting metal oxides play a vital role in many fields of science; like Engineering, Material Science and Physics etc. To achieve oxidic compounds, transition metals make chemical bond with oxygen. Nowadays semiconducting metal oxides are used in the fabrication of piezoelectric devices, as a catalyst, sensors and solar cells. Among semiconducting metal oxides, WO_3 plays a significant importance in electronic devices.

1.5 Introduction to WO_3

A chemical compound that contains three oxygen and one transition metal(tungsten) is known as tungstic oxide or tungstic anhydride or tungsten oxide. The IUPAC name of this compound is tungsten trioxide [49]. Table 1.1 represent different properties of tungsten trioxide.

Table 1.1 Physical properties of WO_3.

Properties	Symbol / Value
Chemical formula	WO_3
Molar mass	231.84 g/mol
Appearance	Canary yellow powder
Density	7.16 g/cm^3
Melting point	1,473 ºC
Boiling point	1,700 ºC
Solubility in water	Insoluble in water

1.5.1 Crystal Structure of WO_3

Tungsten trioxide normally occurs in its most common structure monoclinic. It also occurs in triclinic, orthorhombic and tetragonal structure. WO_3 crystal structure depends upon the temperature [50]. Tungsten trioxide normally occurs in triclinic form in the temperature range of -50 to 17 ºC , it is orthorhombic from 330 to 740 ºC, monoclinic from 17 to 330 ºC and tetragonal at temperature above 740 ºC [51]. Figure 1.7 show the possible structures for tungsten trioxide.

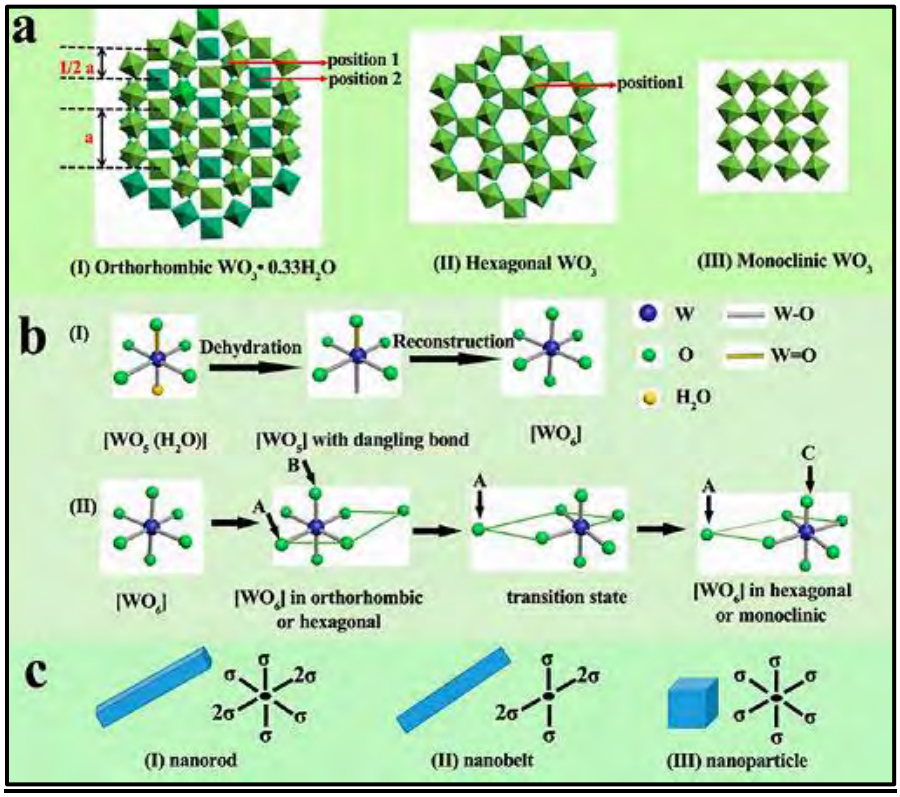

Figure 1.7 (a) WO3 crystal structures in three different forms. **(b)** Tungsten trioxide phase transition process. **(c)** Representation of different types of nanomaterials [52].

1.5.2 Doping in WO_3

The crystal growth of semiconductor is strongly influenced by doping. It not only changes the surface energy but also change the shape and growth directions of the host nanocrystals. In order to get novel properties of material, doping is an easiest approach. After doping in semiconductor, the trace impurities in the primary matrix proficiently changes material properties and sometimes bring novel magnetic, optical and electrical properties in the host material. Due to these tuned properties, these materials are used for various applications. To prepare such materials, numerous strategies have been employed, but that the doping process in semiconductor is not an arbitrary process. Doping process not only depend on primary matrix of

the materials but it also depends on the nature of the dopant ions. The most accepted and useful mechanism through which dopants can be added into the host material is surface adsorption. According to surface adsorption, the binding energy of dopant plays an important role on surface of material. When the impurity ions are adsorbed onto the surface of the host materials, further growth of the nanocrystal is required to stay the impurity ions inside the nanocrystal. If there is slight difference between the host and dopant ions, it creates imperfection at the doping site during doping. In the first case, by the process of self-purification mechanism, the defects will be expelled if the host nanocrystal size is small as compared to the dopant. Secondly, dopant ion will stay inside the host nanocrystal if the free energy change is promising. However, literature detailed study shows that research is mainly engrossed on getting novel properties of semiconductor nanocrystal during doping [53].

Among the metal oxide semiconductors, tungsten trioxide is one of the important and interesting semiconductor with technological potential and a lot of applications like chemical gas sensors, sun roofs, catalysis, antibacterial and smart windows. Due to its small size, simple in function and low cost, the photocatalytic application of tungsten trioxide has many advantages over others [53]. Since we know that a little modification in the size and morphology of nanocrystals plays an important part in determining the nanomaterials physical properties. To modify the geometry, many methods are used now a day. The one which is effective and simple is doping process. During doping process, the dopants or impurities are added to the host lattice network. For the detection of H_2S, Tsai and Tao have doped platinum in Tungsten Trioxide. While for the detection of NO_2, Xia has doped gold in Tungsten Trioxide. While Tesfamichael have investigated the gas sensing behavior for iron doped Tungsten Trioxide for N_2O, NO_2, NH_3 and H_2 gases.

1.6 Graphene and Graphene Nanoplatelets

Recently, a new class of material has been recently discovered which is made from carbon atoms in the form of honeycomb having one atom thick is known as graphene. It has planar morphology in which carbon atoms make bonds with each other's in a hexagonal shape as shown in figure 1.8. Graphene, which is a 2D material can be separated from its parent material graphite. In 1962 Hans Peter Bohem have described single layer carbon foils and named it as graphene, which is formed by the combination of suffix –ene with graphite. First time in 1987, the single sheet of graphite was by graphene. In early days, the term graphene was also used for carbon nanotubes. In graphene, the carbon atoms are sp^2-hybridized. Other allotropes of graphene can also be formed by the extension of honeycomb network of graphene [54]. Stacking of graphene layers result 3D graphite, wrapping of graphene layers form 0D fullerenes and 1D nanotubes can be formed by rolling graphene sheets. Long range π-conjugation in graphene results extraordinary electrical, mechanical and thermal properties. It is considered as one of the thinnest, strongest and lightest material ever discovered in the history of mankind. Since we know that carbon occurs in two different forms i.e. diamond and graphite. Diamond is hard and transparent while graphite is black and soft. Although both materials are made of similar carbon atoms, but the arrangement of atoms make them two different materials. Carbon occurs in many other different forms like fullerenes and graphene with interesting properties [55].

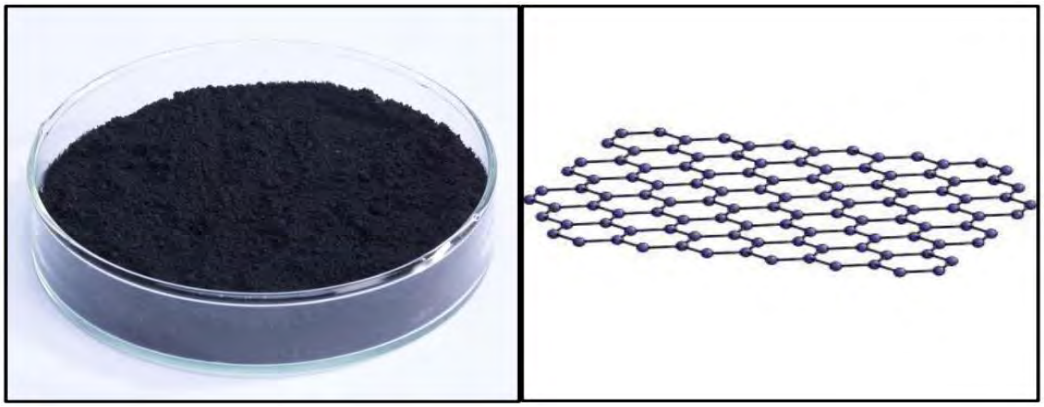

Figure 1.8 Graphene nanoplatelets in powder form and their geometrical shape.

The properties of graphene are unique and extraordinary. Graphene is stronger than diamond as well as from steel. It can be stretched by 20 percent of its original length without breaking. These properties make graphene elastic and stiff. The primary reason is that graphene planes can stretch very simply without any fracture. Due to its super-strong property, graphene is mixed with other materials to make composites and to make them tougher, stronger, lighter and thinner than any material at present. One atom thickness of graphene makes it very thin and light [56]. The mean free path for electrons in graphene is large as compared to other materials, which makes the electrons go further without touching into things. Materials in which such electrons are present can conduct electricity and heat in a best way. The electrons move inside graphene very easily, which makes it good conductor because the honeycomb structure offers slight resistance toward electrons. Hence, graphene shows remarkable conductivity of heat and electricity at normal temperature. The property of graphene that electrons through it move a bit like photons at speed approximately equal to the speed of light and behaves according to theory of quantum mechanics and relativity which is used in electronics and computer chips. The thin material is more transparent as compared to thick one. Single atom thickness of graphene makes

it almost completely transparent. It is due to this reason that graphene transmits 97-98 percent of light. Graphene is impermeable and useful for detecting and trapping gases.

Graphene nanoplatelets are interesting nanosheets, composed of graphene sheets. These sheets are in planar form, platelets like shape and similar to carbon nanotubes planes. The average thickness of graphene nanoplatelets is from 5 to 10 nm and size varying up to 50 μm. Due to its unique morphology and size, mechanical properties like surface hardness, strength and stiffness can be improved. Also, due to the graphitic composition, graphene nanoplatelets are considered as excellent thermal and electrical conductors [57]. GNPs can be found as black powders or granules with 99.5 % carbon content, less than 1 % of oxygen and acid content of 0.5 %. The bulk density of graphene nanoplatelets is 0.03 to 0.1 g/cc. Electrical conductivity of GNPs is 10^7 siemens/m, tensile strength is 5 GPa, tensile modulus is 1,000 GPa, thermal expansion is from 4-6x10^{-6} m/m/dg-k and its thermal conductivity is 3,000 watts/m-k. The surface area of GNPs is 500 m^2/g.

In order to improve the properties of different types of materials like composites, GNPs are best choice to be used due to their unique composition, shape and nanoscale size. Its unique properties can be used but can also be used in combination with other materials to modify the properties. Using GNPs in combination with other materials, one can improve the flame retardance, increase visibility, toughness, stiffness, barrier properties, electrical and thermal conductivities. One can also reduce the component mass to enhance the properties.

1.7 Nanocomposites

Combination of two or more individual materials form a composite. In order to achieve combination of properties, we use the concept of composite materials. Ceramics, polymers and

metals are three different combination of composites. Some of them are natural like wood and bone, while rest of them are man-made like fiberglass etc. Composite materials are sometimes called man-made materials.

Combination of two materials in which one is called matrix phase and the other material is reinforcing phase is known as composites. The reinforcing phase may be particles, fibers or sheets and is rooted in the matrix phase [58]. While composites in which at least one of the dimension is at nanoscale are called nanocomposites. Solid materials that have multiple phase domains and at least one of these domains has in the nanoscale are termed as nanocomposites. Properties of the nanocomposites depend on the interfacial characteristics and morphology of the component materials [59].

The basic idea behind the nanocomposites is to produce and design materials with improved physical properties and flexibility. Since nanocomposites are made from different materials therefore these materials are generally multifunctional. Materials reinforced by nanostructures which are dispersed through the bulk material are termed as nanocomposites. Typically, nanocomposites consist of an organic component and an inorganic solid as a host material. Nanocomposite materials have different structural, optical, catalytic, electrical, electrochemical and mechanical properties which are totally different from those of the individual components. Nanocomposites properties also depend upon the interfaces. High surface area of the nanostructures gives nanocomposites special other properties. Nanocomposites are further divided into two groups: polymer nanocomposites and inorganic nanocomposites. Polymer nanocomposites are characterized by an organic matrix like polymer and reinforced by nanostructures by an organic or inorganic nature like clay. In the second

group, the inorganic matrix like ceramic is reinforced by nanostructures of organic like carbon-based material or by inorganic nature like metals.

Since we know that materials having magnetic properties are used nearly in all technical fields like household applications, space operations, materials testing, aviation, telecommunication, computer elements, high power electromotors, mechanical power, sensor techniques and electrical power etc. When size of the bulk magnetic materials are reduced to nanoscale results to hard or soft magnets with highly improved properties. For example, Finemet which is an Fe-Si-B alloy with low amount of Cu and Nb. After annealing the Finemet at temperatures above the crystallization temperature, its amorphous phase change to crystalline solid with grain size of about 10 nm. This alloy has large value of permeability, outstanding magnetic induction and small value of coercive field. To improve the magnetization curve of permanent magnets, one need to fabricate nanocomposite. For such type of nanocomposite, the hard-magnetic phases are reinforced in soft magnetic matrices like soft α-phase of iron. The idea behind this is to increase the remnant field. By reducing the size of the grains in the magnetic material, we can increase the energy product. The energy product is the product of the coercivity and magnetization. To reduce the grain size coercivity increases correspondingly. One of the best example is magnetic multilayer nanocomposites, which are the important component of new generation data storage device. For example, magneto-resistive random-access memory (MRAM).

1.8 Applications of Graphene-Tungsten Oxide Nanocomposites

Graphene-tungsten trioxide nanocomposites is expected to be one of the most effective photocatalysts. Owing to the graphene exceptional properties, these nanocomposites have

publicized an outstanding achievement. Using lunar energy, these nanocomposites have pinched an important consideration in the field of photo-active chemical change. Enhancement of the photocatalysts chemical firmness, enrichment of active surface locations, growth of light intensity absorption, increase the range of light absorption and decrease of electron-hole pairs recombination rate have been needed to trigger the photocatalytic property of graphene-tungsten oxide nanocomposites [60]. In this research, the development of graphene-tungsten trioxide nanocomposites has been emphasized, concentrating on the process of enhanced photocatalytic activity on degradation of organic dyes and antibacterial applications. The photocatalytic effect of WO_3 nanoparticles on graphene nanoplatelets has been highly evaluated in the research work. Methyl blue dye has been selected for photocatalysis because of large amount usage in industries and its harmful effects on human and other aquatic living organisms.

Recent progress in graphene-tungsten oxide nanocomposites have been planned for water decontamination from pathogenic bacteria [61]. Antibacterial activity of these nanocomposites may rest on numerous aspects; i.e. concentration of the sample, nature of microorganism, production of oxygen species and morphology of the samples. Keeping in mind these features, an effort has been made to fabricate novel nanocomposites to enhance the antibacterial properties of both graphene and WO_3 nanostructures for growth inhibition of bacteria. Antibacterial bacterial activity has been performed against two most hazardous bacterial species; *Staphylococcus epidermidis* and *Klebsiella pneumoniae*.

1.9 Aims and Objectives

The aims of the research work are;

- To synthesize the nanocomposites with controlled morphology using modest and profitable way.
- Modifying of the physical properties for the nanocomposites using Fe metal doping to boost their antibacterial activity and photocatalytic properties.
- Optimization of various mixture parameters like pH of the solution and reaction temperature etc. for fine nanocomposites at bulk industry level.
- Examining the morphological, photosensitive, vibrational and physical properties of the nanocomposites.
- Investigating the photocatalytic activity of these nanocomposites against different dyes.
- Inspecting the nanocomposites against both the *Staphylococcus epidermidis* (Gram-positive bacteria) and *Klebsiella pneumonia* (Gram-negative bacteria).

Chapter No.2

Synthesis Techniques

The properties of nanomaterials depend upon the morphology, crystal structure and synthesis techniques. There are several physical and chemical methods to synthesize nanomaterials depending upon the particle size distribution and stoichiometry of the nanostructures. The two approaches for synthesis of nanostructures are as follows:

2.1 Top-down Approach

According to top down approach, nanomaterials are made by taking a macroscopic structure initially which is then reduced to nanoscale by an externally controlled processing. For example, lithographic techniques and ball milling are top down approaches. Top down approach means from larger to smaller. In this approach, a bulk piece of material is taken, cutting and carving is done until the desired nanostructures are achieved. This approach is naturally not very quick and cheap. Through this approach, large scale production is not possible and at very slow rate.

2.2 Bottom-up Approach

In this approach, a nanometric or an atomic structure is taken using the methods of assemblage procedure, to develop nanostructures. Bottom up approach means from smaller to larger. During the self-assembly, at nanoscale, elementary units combine to form bigger units with the help of physical forces. Nanoparticles formation by colloidal diffusion is one of the best example of bottom up approach. In this approach, the molecules or atoms in solution form are

taken and are used to build up the corresponding nanomaterials. Bottom up approach is less expensive [62]. The schematic representation of both approaches is shown in figure 2.1.

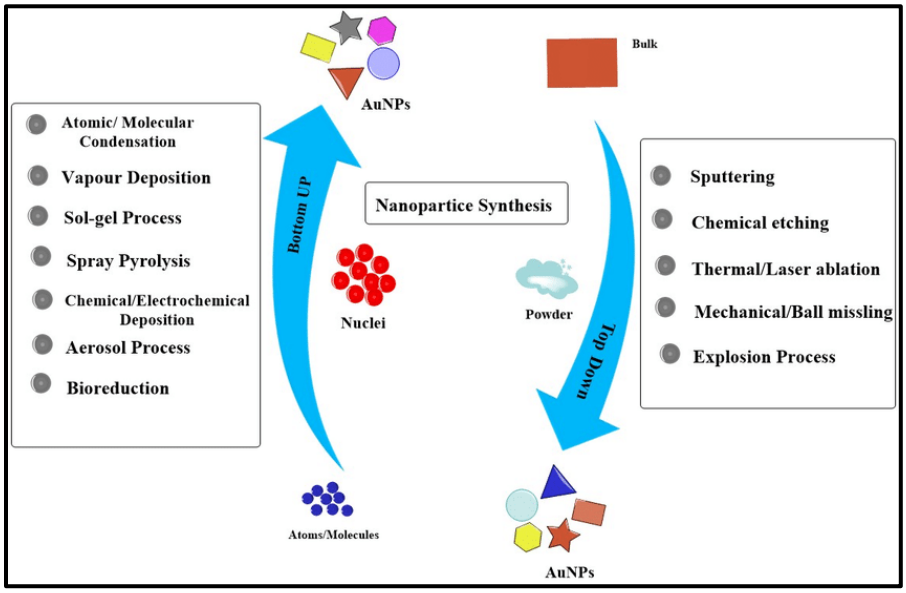

Figure 2.1 Two techniques for the preparation of nanoparticles.

2.3 Chemical Synthesis Methods

There are several chemical methods for synthesis of nanomaterial's depending upon the temperature range. The most common chemical methods are: hydrothermal, co-precipitation, sputtering, thermal evaporation, sol–gels and chemical vapor deposition etc. In this research work, chemical co-precipitation method has been used because it is very simple, and the temperature required during the chemical reaction is low. The metal cations are normally co-precipitated from the oxides, carbonates or hydroxide as a given precursor for the required material. Practically, oxides or carbonates of the related metals are taken and digested with acid. To obtain the ultimate product, the precipitates are calcined at proper temperature. During the chemical reaction, atoms are mixed with each other to form particles but due to the small value for calcination temperature, particle size also remains small. To get the final powder with

required properties, various parameters like reaction temperature, stirring speed, pH value and concentration of the solution must have controlled.

2.4 Synthesis of $Fe_xW_{1-x}O_3$ (x= 0, 3, 5, 7 & 10) Nanoparticles

WO_3 nanoparticles with different Fe doping concentration have been synthesized via chemical co-precipitation method. During preparation, the hydrochloric acid has been used to adjust the pH of the solution. Sodium Chloride as capping agent and sodium tungstate dihydrate ($Na_2WO_4.2H_2O$) has been used as a precursor. Different molar ratios of $FeCl_3.6H_2O$ and $Na_2WO_4.2H_2O$ have been dissolved into 57 ml distilled water to get 0, 3, 5, 7 and 10 % Fe doped WO_3 nanoparticles. After dissolution of these precursors, 1.16 g of sodium chloride has been added. Then three molar hydrochloric acid solutions have been added drop wise to the first solutions through constant stirring until pH value reached to 1. Furthermore, the solution has been centrifuged three times to accumulate the required precipitates. Using distilled water, the precipitates have been washed three times. The as-prepared samples have been dried out for 16 hours at 80 ºC. Finally, the samples have been annealed in furnace for 2 hours at 600 ºC. The flowchart for the overall process is shown in figure 2.2. The chemical reactions for the formation of crystalline structures of tungsten trioxide are given below;

$$Na_2WO_4 + 2HCl \rightarrow H_2WO_4 + 2NaCl \quad (2.1)$$

$$H_2WO_4 \rightarrow WO_3 + H_2O \quad (2.1)$$

$$WO_3(Amorphous) \rightarrow WO_3(Crystalline) \quad (2.3)$$

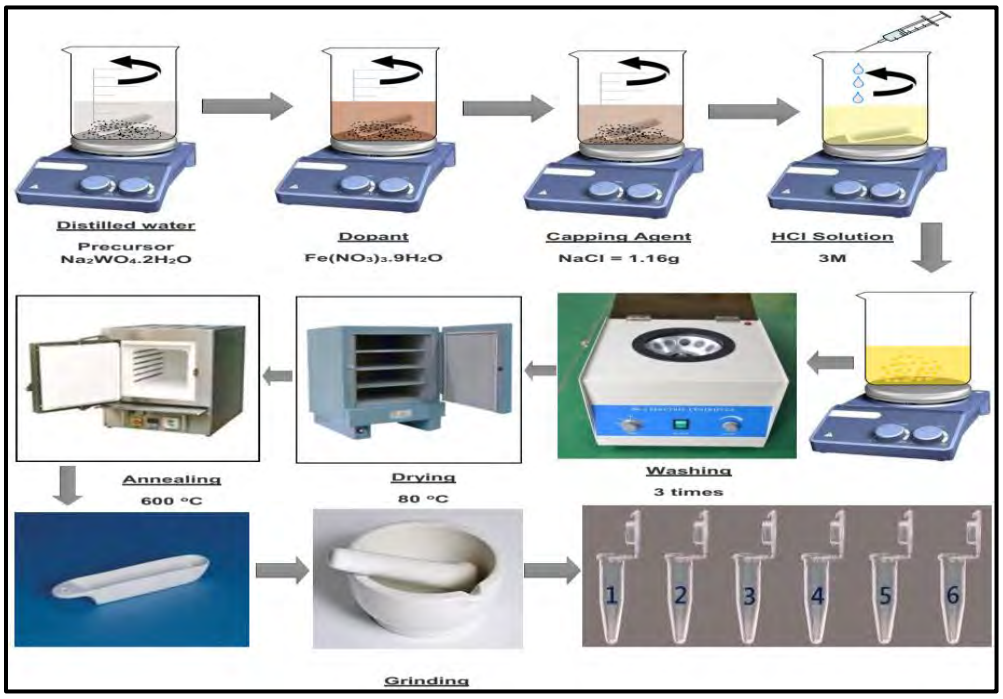

Figure 2.2 Flow chart for FexW1-xO3 (x= 0, 3, 5, 7 & 10) nanoparticles.

2.5 Synthesis for $(Fe_xW_{1-x}O_3)_{0.5}(GNPs)_{0.5}$ {x= 0, 3, 5, 7 & 10} Nanocomposites

In order to synthesis $(Fe_xW_{1-x}O_3)_{0.5}(GNPs)_{0.5}$ {x= 0, 3, 5, 7 & 10} nanocomposites ex-situ method has been employed. $Fe_xW_{1-x}O_3$ (x= 0, 3, 5, 7 & 10) nanoparticles has been synthesized using chemical co-precipitation method whiles GNPs has been purchased (99.9% KNano). Fe doped WO_3 nanoparticles were added to 100 ml distilled water and sonicated for 2 hours. GNPS were also taken in a separate beaker and sonicated for 2 hours. After sonication the two solutions were mixed and stirred for 1 hour. The as-prepared solution was dried for overnight and calcined at 600 ºC for 2 hours. The required nanocomposites were grinded finely to get the required powder and forwarded for further characterizations. The flow chart for the whole process is shown in figure 2.3.

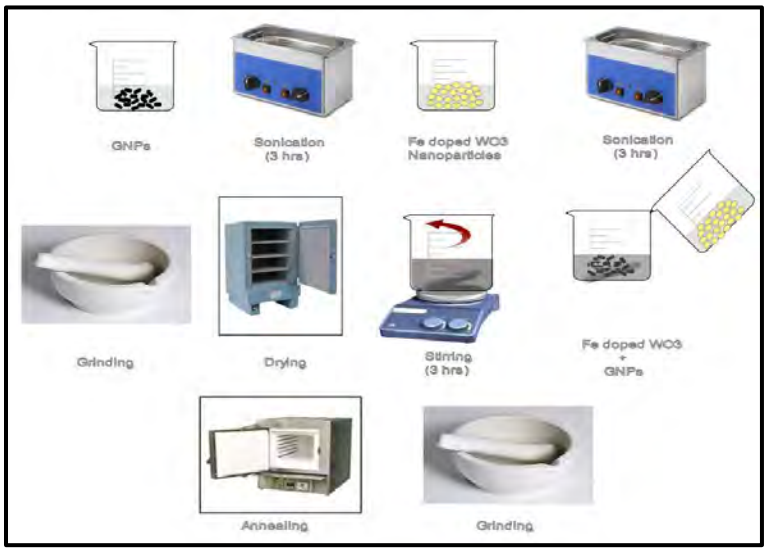

Figure 2.3 Flow chart for (FexW1-xO3)0.5(GNPs)0.5{x= 0, 3, 5, 7 & 10} nanocomposites.

During sample preparation by co-precipitation method, the following instruments have been used;

2.5.1 Hot Plate and Magnetic Stirrer

During the synthesis of WO_3 nanoparticles and its nanocomposites the reactants need to be mixed homogeneously. For this purpose, the hot plate and magnetic stirrer have been used. Normally the magnetic stirrers are magnetic bars which are immersed in the suspension during the sample preparation. These magnetic bars continuously rotate in the suspension. The revolutions per minute (rpm) of the magnetic stirrer is well regulated. The hot plate on the other hand is used for desirable temperature during the chemical reaction.

2.5.2 Electric Oven and Furnace

Series thermal-electric thermostatic drying oven; model DHG-9202; 30 L has been used for heat treatment and for drying the as-synthesized samples. The temperature inside the oven

has been kept 80 ºC for 16 hours. In order to achieve the required crystalline phase of WO_3 nanoparticles, annealing of the samples have been done in an electric furnace (model RLF 160/3 ALSER TEKNIK).

2.6 Experiment for Photocatalysis

The photocatalytic activity of all the samples has performed for degradation of methyl blue (MB). For Stock solution, 10 mg of MB was taken and homogeneously dispersed followed by stirring for 15 min in 1litre of distilled water. 5 mg of each photocatalyst was mixed with 50 ml of MB solution in a beaker taken from the stock solution and kept under stirring in dark for adsorption-desorption for 50 min. The UV light was then exposed to each sample after complete equilibrium of adsorption-desorption. Each experiment was performed under UV exposure for total time of 3 hrs. The concentration of dye was noted with photo spectrometer by taking 5 ml aliquots with the help of dropper after every 20 min.

2.7 Antimicrobial Properties

Antibacterial activity was checked against both the bacterial species; Gram-positive and Gram-negative bacteria (*Staphylococcus epidermidis* and *Klebsiella pneumoniae*), by MHA agar gel diffusion assay. 0.1 mg from all the samples (undoped WO_3, Fe doped WO_3 and their nanocomposites) have been taken and dissolved in distilled water and labelled properly. The solution has then allowed to sonicate for 1 hour at room temperature. After sonication the samples were transferred to Microbiology lab, department of microbiology, QAU, Islamabad, Pakistan. Volume of 100 µL from each sample was poured into the wells in MHA (Muller Hinton Agar) plate through a micropipette. Antibacterial activity has been carried out in the

biological safety cabinet. Petri plates then placed at 37 ^{o}C for 24 hours in incubator. After incubation ZOIs were measured.

Chapter No.3

Characterization Techniques

For the study, and verification of nanocomposites, many experimental methods and techniques are used recently. To investigate the crystal structure of our samples, X-ray diffraction has been performed using X-ray diffraction. Morphology of the $(Fe_xW_{1-x}O_3)_{0.5}(GNPs)_{0.5}$ {x= 0, 3, 5, 7 & 10} nanocomposites has been checked by scanning electron microscope, bandgap by Ultraviolet visible diffuse reflectance spectroscopy and functional group by Fourier transform infrared (FTIR) spectroscopy.

3.1 X-Ray Diffractometer (XRD)

XRD is an instrument which is used for identification and determination of the crystallinity of solids. During the analysis, monochromatic X-ray beams is incident on the sample, after which it diffracts from the sample like diffracting grating over a specific range of angles, various diffraction peaks with their corresponding intensities give the evidence about the sample crystal structure. To check the crystallinity of samples D8 ADVANCE Bruker system has been used which operates at 40 keV of voltage and 30 mA of current. The X-ray source in this instrument was Cu with wavelength Cu-k_α equal to 1.54 Å.

There are mainly three parts of X-ray diffractometer; a sample holder, an X-ray source and a counter. For an XRD, the sample is normally in powder form. Since powder sample (polycrystalline) consists of many fine and randomly arranged particles subjected to X-ray source through sample holder. As each grain or powder particle is a crystal, having many unit

cells, their random orientation makes them possible for XRD to establish the crystallographic planes. At the opposite side of X-ray source, a monochromator is placed to have X-ray beam monochromatic. The counter, X-ray source and the specimen are all in same plane. The counter is mounted on a movable carriage. The specimen and carriage are fixed such that turning of the counter through 2θ is accompanied by a θ rotation of the specimen. To maintain focused and well-defined beam, collimators are placed in front of X-ray beam. The counter when rotates with angular velocity; peaks intensity versus angle (2θ) is recorded by the recorder [63]. The pictorial representation of XRD set-up is shown in figure 3.1.

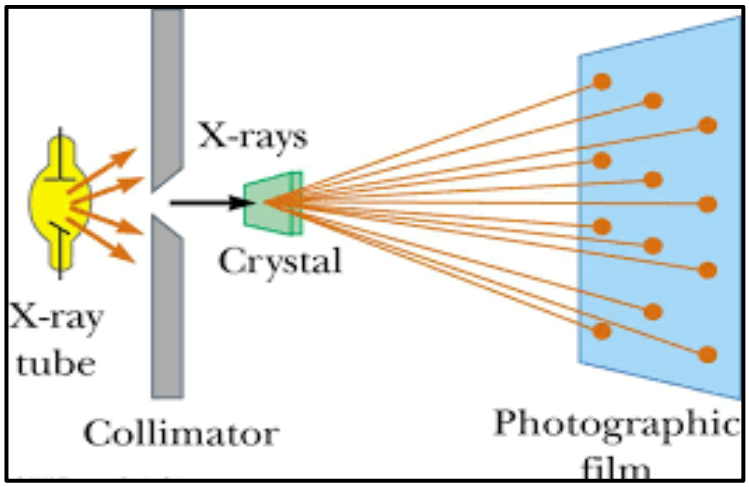

Figure 3.1 Pictorial representation of XRD set up.

Since every crystal has periodic arrangement of atoms, hence, diffract electromagnetic radiation of specific wavelength. When the wavelength of the incoming wave is equal to the interplanar spacing then diffraction phenomenon will occur. As the wavelength of X-rays and the interplanar spacing in crystals both are in Angstrom (Å). Therefore, X-rays can be diffracted from crystalline solids. X-rays beam when incident on the sample, scattered in different

directions. Due to the constructive interference of diffracted waves, diffraction peaks can be seen in the XRD pattern. No diffraction peak has ever been observed for destructive interference.

3.1.1 Working Principle of XRD

Bragg's law is the basic principle of XRD. For constructive interference of X-rays, Bragg's law can be expressed as

$$n\lambda = 2dsin\theta \tag{3.1}$$

Where θ, d, λ and n represent the incident angle, interplanar spacing, wavelength of X-rays and order of diffraction respectively.

For the determination of lattice parameters, one need to calculate the following from Bragg's law. Using the Bragg's law find the interplanar spacing 'd'. From the peaks identify the Miller indices (hkl). Also find the location of angle 2θ. Using the required crystal structure formula and use the corresponding formula which shows the relation between the lattice parameters and interplanar distance.

To find the average crystallite size of the particles from the measured width of the diffraction curves we use the Scherrer's formula. The Scherrer's formula is

$$< d >= \frac{k\lambda}{\beta cos\theta} \tag{3.2}$$

Where θ, β, λ, k and d represent the Bragg angle, full width at half maxima (FWHM), X-ray wavelength, Scherrer constant and mean size of the crystal. The value of Scherrer constant is 0.9. typically, the crystallite size is determined from the peaks having maximum intensity in XRD pattern. Then the average is taken to find the approximate crystallite size.

3.2 Scanning Electron Microscopy (SEM)

For the morphological study of a sample we use scanning electron microscope. This technique is used for microstructural study. From the SEM, we get the image to check and verify it in nanoscale. SEM is the best technique to get information about the grain size, microstructural and morphology of the materials [64]. Schematic representation of SEM is shown in figure 3.2.

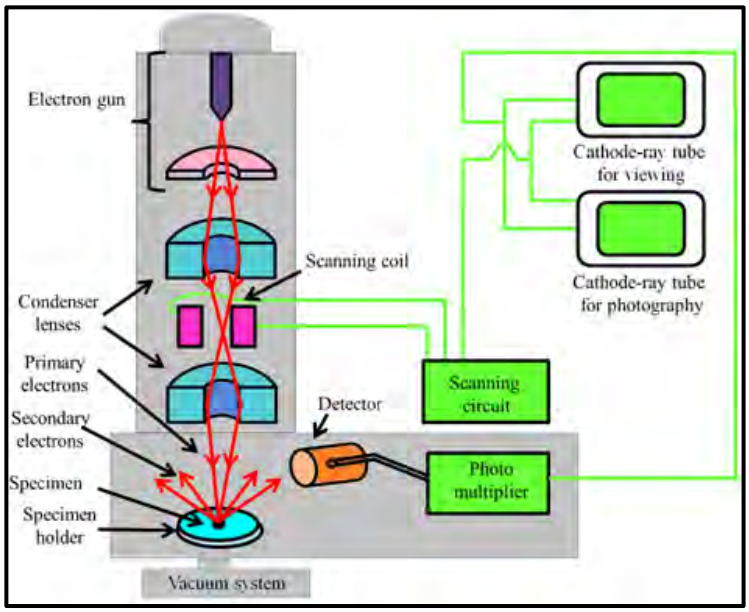

Figure 3.2 Scanning Electron Microscopy set up at UOP, Peshawar.

The basic principle behind the SEM is the interaction of electrons with matter. Since there are two types of interactions; elastic and inelastic interactions. During the inelastic interaction, electrons having high energy interact with the sample and transfer its energy to the atoms of the sample. Which result ionization of the atoms of samples and emit the secondary electrons. In elastic interaction incident electrons are deflected by outer electron or nuclei of the atoms of samples. When these electrons are expelled from the surface of the sample, produce signals in SEM which are then used to study the topographic feature of the sample. Among these

two types of signals other signals like X-ray and auger electrons are also produced. SEM further utilize these signals, for surface and below the surface topographies of the sample.

SEM has two major components; one is the optical column and second is sample chamber. The optical chamber contains the assembly to focus the electron on the sample, therefore its size is small. At the top of the optical column, an electron gun is situated to produce electrons. The source produce electron beams of large diameter, therefore apertures and electromagnetic lenses are used to de-magnify it. Beneath the optical column a sample chamber is located. To use the sample chamber easily, it has large size as compared to optical chamber. Apart from this a vacuum pump is used to produce a high vacuum environment, so that electron beam reaches the sample easily without any disturbance. Signals are produced when electron beam interact with samples. These signals are captured by the detector and send forward to the display; hence, image is formed. The images formed can be recorded.

3.3 Ultraviolet Visible Defuse Reflectance Spectroscopy (DRS)

Measurement of the absorptivity, reflectivity, intensity and spectral distribution of the infrared, ultraviolet and visible radiation which are emitted, reflected from and pass through the sample is known as optical measurement. Many devices are used to measure the spectral measurement. To measure the optical properties, especially to measure the bandgap we use the photo spectrometer. The bandgap can be calculated from the reflectance spectra.

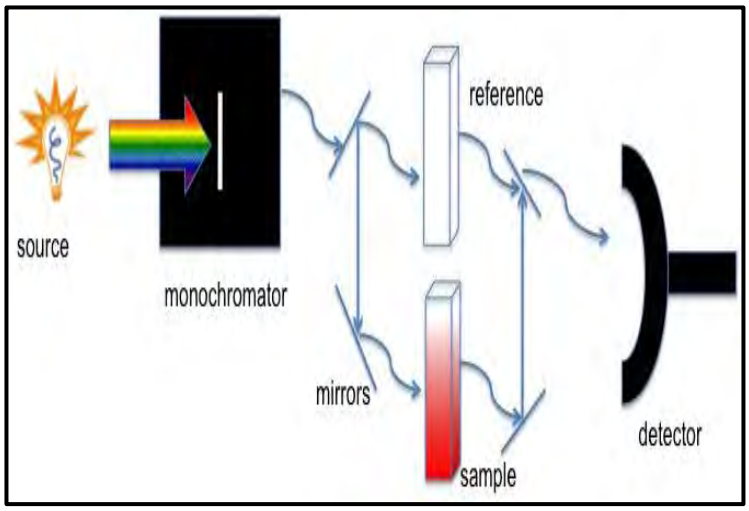

Figure 3.3 UV-vis photo spectrometer.

To measure the optical properties of a sample, versatile lambda 950 spectrometer is used normally. This instrument has the advantage to operate in near infrared (NIR), visible and ultraviolet regions. The light source in this device is usually tungsten-halogen and deuterium. While photomultiplier and PbS tube are used for the detection of NIR and complete range of UV/Vis.

Lambda 950 spectrometer consists of four windows and all compartments are sealed. Sample compartment window is normally made of silica which provides protection from dust and fumes.

3.4 Fourier Transform Infrared Spectroscopy (FTIR)

Spectroscopy is one of the best characterization that is used to know about the different characteristics of molecules and atoms in a given material. To know about the organic molecules, infrared spectroscopy is normally used these days by chemists. Old-style spectroscopy consists of an optical element, such as diffraction grating which blowouts out several wavelengths in an intricate optical signal from the material into various angles. Hence, the different wavelengths of

radiation and their intensities in the signal can be examined. These sorts of instruments are restricted in their firmness and efficiency because they must be skimmed through the several angular deviations of the radiation.

One of the best method for infrared (IR) spectroscopy is Fourier transform infrared (FTIR) spectroscopy. A beam of infrared (IR) radiation is incident on a given sample, some of the radiation passes through it while others are absorbed by the sample. Infrared region normally occurs in the range from 10 cm^{-1} to 12800 cm^{-1}. IR region is further divided into three parts; far-IR region which is from 50 cm^{-1} to 1000 cm^{-1}, near-IR region which is from 12800 cm^{-1} to 4000 cm^{-1} and mid-IR region (4000 cm^{-1} to 200 cm^{-1}). The frequently used infrared spectra for absorption spectroscopy is from 400 cm^{-1} to 4000 cm^{-1}. The reason is, most of the inorganic and organic compound ions lies in that region. To know the molecular fingerprint of the sample, the resulting signal at the detector shows the required spectrum. The practicality of IR spectroscopy rises because different molecules creates dissimilar spectral patterns.

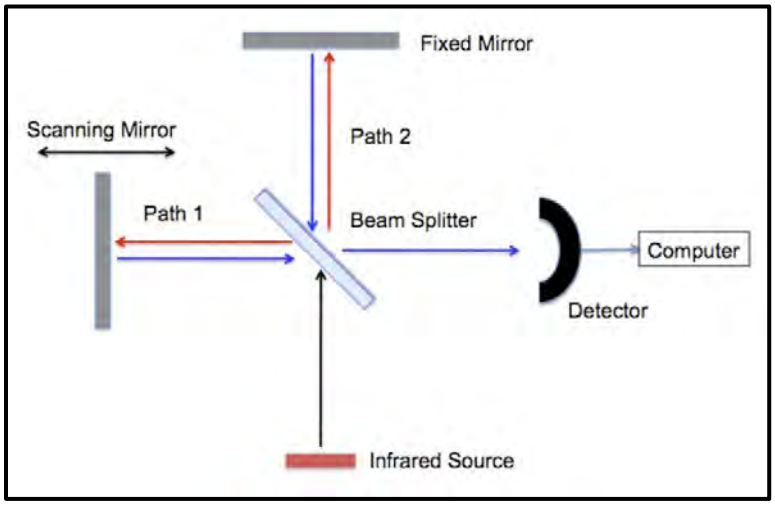

Figure 3.4 Fourier Transform Infrared Spectrometer setup.

3.5 Photocatalytic Degradation of Methyl Blue (MB)

The photocatalytic degradation activities for $(Fe_xW_{1-x}O_3)_{0.5}(GNPs)_{0.5}\{x= 0, 3, 5, 7 \& 10\}$ nanocomposites, were studied for the degradation of methyl blue under UV light irradiation. An indigenous photocatalytic chamber has been arranged for photocatalysis of MB in which 90 W, C-type UV lamp was used as irradiation source. During the experiment, 5 mg of the photocatalyst $(Fe_xW_{1-x}O_3)_{0.5}(GNPs)_{0.5}\{x= 0, 3, 5, 7 \& 10\}$ were added in 50 mL of an aqueous methyl blue solution with 10 mg/L concentration followed for 15 min stirring in the dark. The distance between the UV lamp and the MB solution containing catalyst was kept 16 cm. The MB degradation experiments were performed for 3 hours. Using a micropipette, 2 mL solution was taken at regular interval after every 20 min for taking the UV-vis absorption range. The degradation of MB dye was plotted as a function of irradiation time by UV-vis spectrophotometer. From the degraded solutions, the decrease in absorbance was calculated for MB photodegradation. The percentage were calculated using the expression;

$$Photodegradation\ (\%) = \frac{C_o - C}{C_o} x100 \tag{3.5}$$

Where C_o represents initial concentration of *MB* before irradiation and *C* shows the concentration of *MB* after a specific time of UV irradiation.

Chapter No. 4

Results and Discussions

This section is mainly concerned with the various techniques employed at different stages for the characterization of $(Fe_xW_{1-x}O_3)_{0.5}(GNPs)_{0.5}\{x= 0, 3, 5, 7 \& 10\}$ nanocomposites. This chapter includes results and discussions of several characterization tools employed for the optical, morphological and structural characterization of nanocomposites. The focus will be on the instrumentation, understanding of fundamental principle and supportive tools offered for the characterizations.

4.1 Structural Analysis of Nanocomposites

To check the crystallinity of the prepared samples, XRD pattern has been obtained from the X-ray diffractometer. Figure 4.1 represents the XRD patterns for $(Fe_xW_{1-x}O_3)_{0.5}(GNPs)_{0.5}\{x= 0, 3, 5, 7 \& 10\}$ nanocomposites with fixed ratio of GNPs in each sample. The XRD pattern displays that major peak for GNPs lies at an angle of 26.46º and for WO_3 these peaks lie at 23.08º, 23.61º and 24.36º. In case of nanocomposites, the GNPs and WO_3 peaks overlap at 26.60º and confirm the presence of both materials [65]. The obtained diffraction peaks are in agreement with the JCPDS card 043-1035 to the monoclinic crystal structure of WO_3. The X-ray diffractogram confirms the multiphase formation of the $(Fe_xW_{1-x}O_3)_{0.5}(GNPs)_{0.5}\{x= 0, 3, 5, 7 \& 10\}$ nanocomposites.

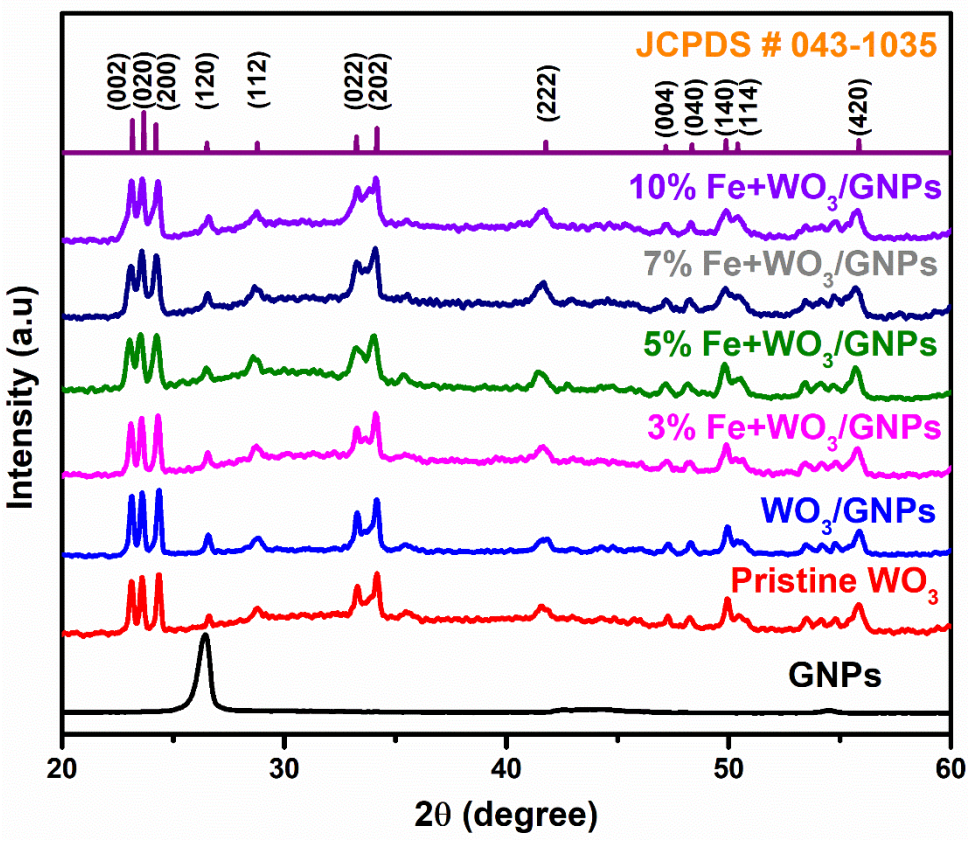

Figure 4.1 XRD patterns of (FexW1-xO3)0.5(GNPs)0.5{x= 0, 3, 5, 7 & 10} nanocomposites.

No extra peaks associated to any other impurities or dopant has been institute in the XRD pattern which shows the complete incorporation of Fe in WO_3 crystal structure. Furthermore, as the Fe concentration increases, the peak shifts occur toward the lower angle values. In addition, the decrease in peak intensities can also be seen from the XRD pattern with the increase of Fe concentration. The peak shifts can be easily observed from Figure 4.2.

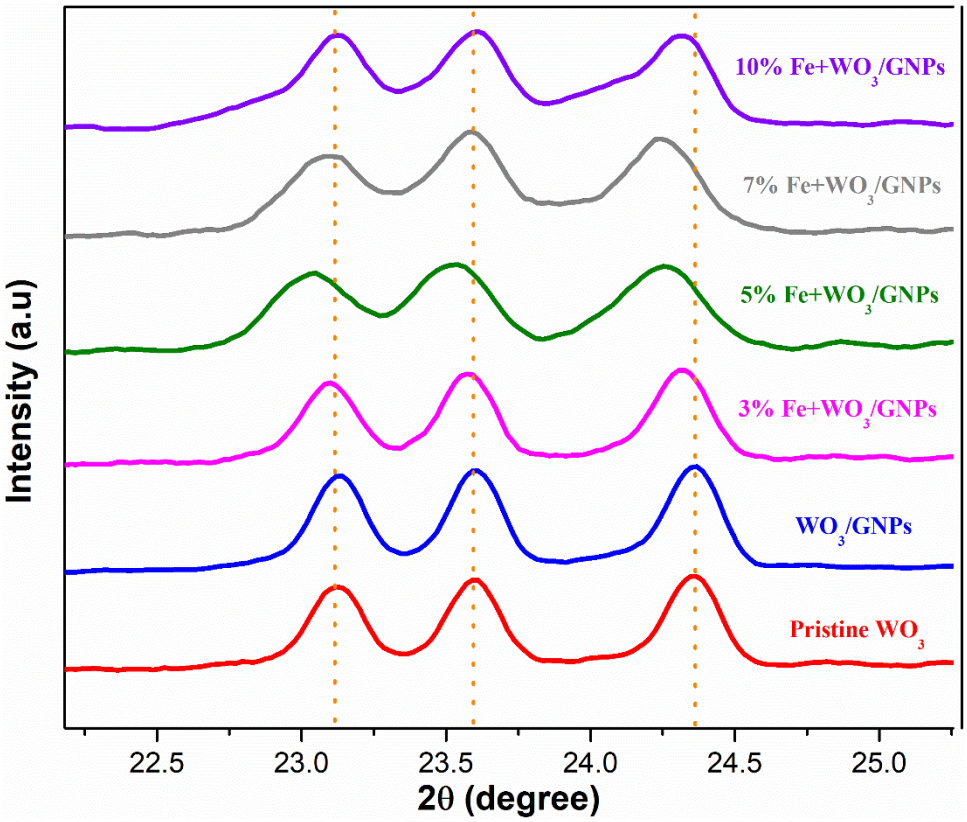

Figure 4.2 XRD prominent peaks shift for (FexW1-xO3)0.5(GNPs)0.5{x= 0, 3, 5, 7 & 10} nanocomposites.

The peak shifts have been observed by the varying concentration of Iron ions. Since there is small change between dopant Fe^{3+} (0.64 Å) and ionic host W^{6+} (0.62 Å) radii. Therefore, Fe^{3+} ions can be replaced in the host matrix of W^{6+} ions. With the increase in Fe concentrations, decrease in the intensities as well as peak broadening is observed in the pattern. The decrease in peak intensities occur by the poor crystallinity and small crystallite size. The peaks broadening results due to lattice strain and instrumental effects.

4.1.1 Average Crystallite Size

The average crystallite size for $(Fe_xW_{1-x}O_3)_{0.5}(GNPs)_{0.5}${x= 0, 3, 5, 7 & 10} nanocomposites have been calculated using the Debye-Scherrer formula:

$$D = \frac{k\lambda}{\beta cos\theta} \tag{4.1}$$

Equation 4.1 is known as Debye-Scherrer formula in which *k, β, λ, θ* and *D* represents the shape factor, full width at half maximum, wavelength for X-rays and size of crystallite respectively. The approxiamte values for *k* and *λ* are 0.9 and 1.54 nm respectively. The average crystallite size has been calculated from Debye-Scherrer equation using three major peaks for the planes (002), (020) and (200) at an angle of 23.08º, 23.61º and 24.36º respectively.

Table 4.1 Average crystallite size for $(Fe_xW_{1-x}O_3)_{0.5}(GNPs)_{0.5}${x= 0, 3, 5, 7 & 10} nanocomposites.

S. No	Crystallite Size for (002) Peak (nm)	Crystallite Size for (020) Peak (nm)	Crystallite Size for (200) Peak (nm)	Average Crystallite Size (nm)
WO_3	48.12	40.41	46.12	44.8
$(Fe_xW_{1-x}O_3)_{0.5}(GNPs)_{0.5}$	48.12	40.41	46.12	44.8
$(Fe_xW_{1-x}O_3)_{0.5}(GNPs)_{0.5}$ {x= 3}	41.60	48.58	48.61	46.26
$(Fe_xW_{1-x}O_3)_{0.5}(GNPs)_{0.5}$ {x= 5}	42.01	45.32	46.20	44.51
$(Fe_xW_{1-x}O_3)_{0.5}(GNPs)_{0.5}$ {x= 7}	44.21	44.62	47.52	45.45
$(Fe_xW_{1-x}O_3)_{0.5}(GNPs)_{0.5}$ {x= 10}	45.09	45.13	54.21	48.14

Table 4.1 shows the crystallite size calculated for three major peaks of the $(Fe_xW_{1-x}O_3)_{0.5}(GNPs)_{0.5}${x= 0, 3, 5, 7 & 10} nanocomposites. From the table 4.1, the average crystallite size varies with different Fe concentrations. For 10 % Fe doped WO_3 the average crystallite size is greater as compared with other samples. The lowest average crystallite size is observed for undoped WO_3 nanoparticles. This is due to the slight mismatch of the lattice.

4.1.2 Lattice Parameters

For the monoclinic phase of $(Fe_xW_{1-x}O_3)_{0.5}(GNPs)_{0.5}${x= 0, 3, 5, 7 & 10} nanocomposites, the lattice constants *a*, *b* and *c* has been calculated using formula for monoclinic structure. The lattice constant *a* has been calculated from (200), *b* from (020) and *c* from (200) plane respectively.

Table 4.2 Lattice constants value for each sample.

Name of the Sample	Lattice Parameter for (200) Peak *a* (Å)	Lattice Parameter for (020) Peak *b* (Å)	Lattice Parameter for (002) Peak *c* (Å)
WO_3	7.30	7.54	7.68
$(Fe_xW_{1-x}O_3)_{0.5}(GNPs)_{0.5}$	7.30	7.54	7.68
$(Fe_xW_{1-x}O_3)_{0.5}(GNPs)_{0.5}$ {x= 3}	7.30	7.54	7.70
$(Fe_xW_{1-x}O_3)_{0.5}(GNPs)_{0.5}$ {x= 5}	7.31	7.53	7.69
$(Fe_xW_{1-x}O_3)_{0.5}(GNPs)_{0.5}$ {x= 7}	7.32	7.54	7.71
$(Fe_xW_{1-x}O_3)_{0.5}(GNPs)_{0.5}$ {x= 10}	7.32	7.52	7.69

All the lattice constant values (*a*, *b* and *c*) in table 4.2 agree with the reported values. The lattice parameters *a*, *b* and *c* affirm the monoclinic phase of undoped and Fe doped WO_3 respectively.

4.2 Morphological and Microstructural Analysis

For the morphological and microstructural analysis of $(Fe_xW_{1-x}O_3)_{0.5}(GNPs)_{0.5}${x= 0, 3, 5, 7 & 10} nanocomposites, SEM micrograph has been captured for all samples. The afore mentioned samples have been characterized using scanning electron microscopy (SEM, JSM-JEOL) operated at voltage of 15 kV. Using the ***Image J software,*** the particle size and its

diameter have been calculated by analyzing the microstructural images obtained from the SEM. For single phase formation, the calcination temperature of the samples has been maintained at 600 ºC.

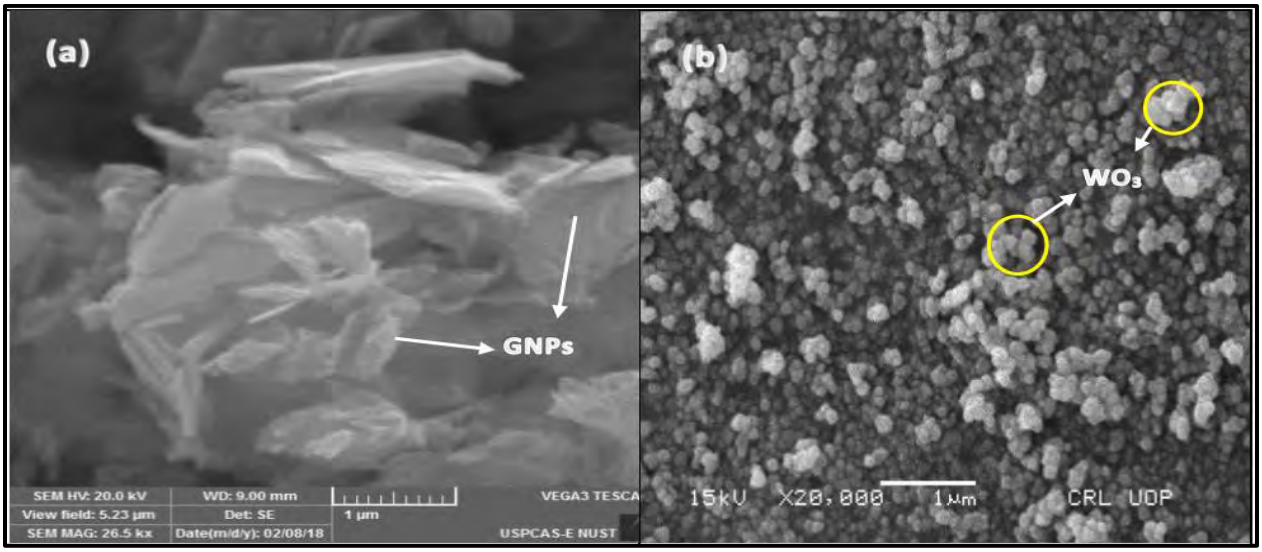

Figure 4.3 SEM images for (a) Graphene nanoplatelets and (b) Undoped WO3 nanoparticles.

SEM images in figure 4.3 (a) depicts the plates like morphology of GNPs and (b) suggest the spherical morphology of the pristine WO_3. The average diameter for undoped WO_3 is 75 nm, in the range of 40-122 nm. SEM micrograph in figure 4.4 (c) reveal the multiphase nature of material by the formation of WO_3 nanoparticles on GNPs. WO_3 nanoparticles seem to be embedded on GNPs. Figure 4.4 (d) is the SEM image of $(Fe_xW_{1-x}O_3)_{0.5}(GNPs)_{0.5}\{x= 3\}$ nanocomposites [66].

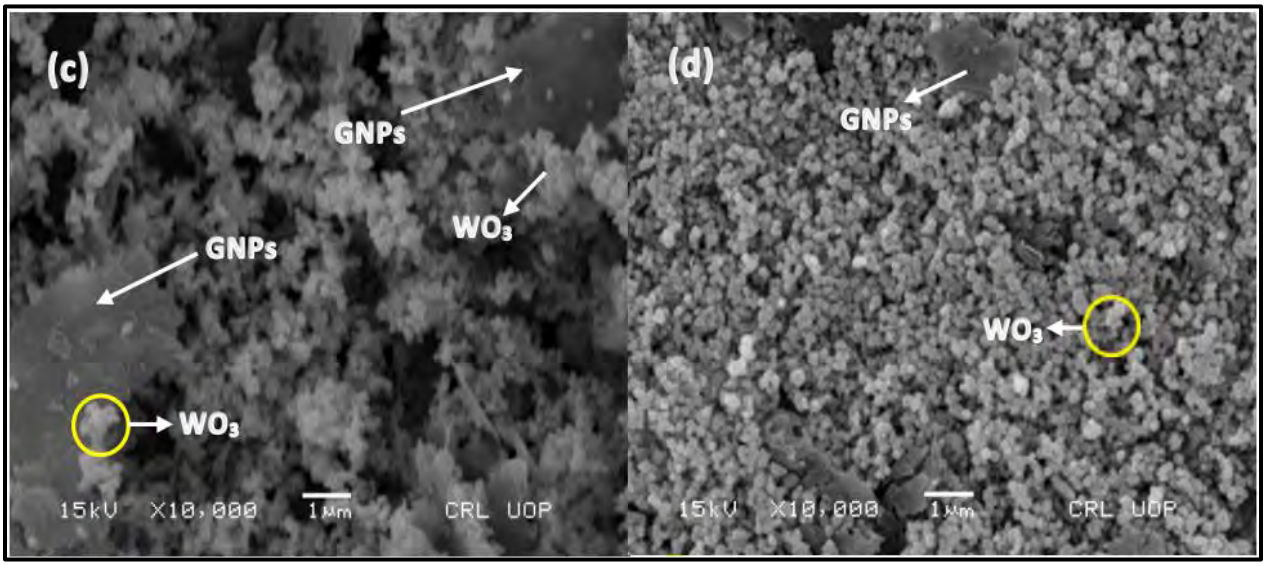

Figure 4.4 SEM micrographs for **(c)** (WO3)0.5(GNPs)0.5 and (d) (FexW1-xO3)0.5(GNPs)0.5{x= 3} nanocomposites.

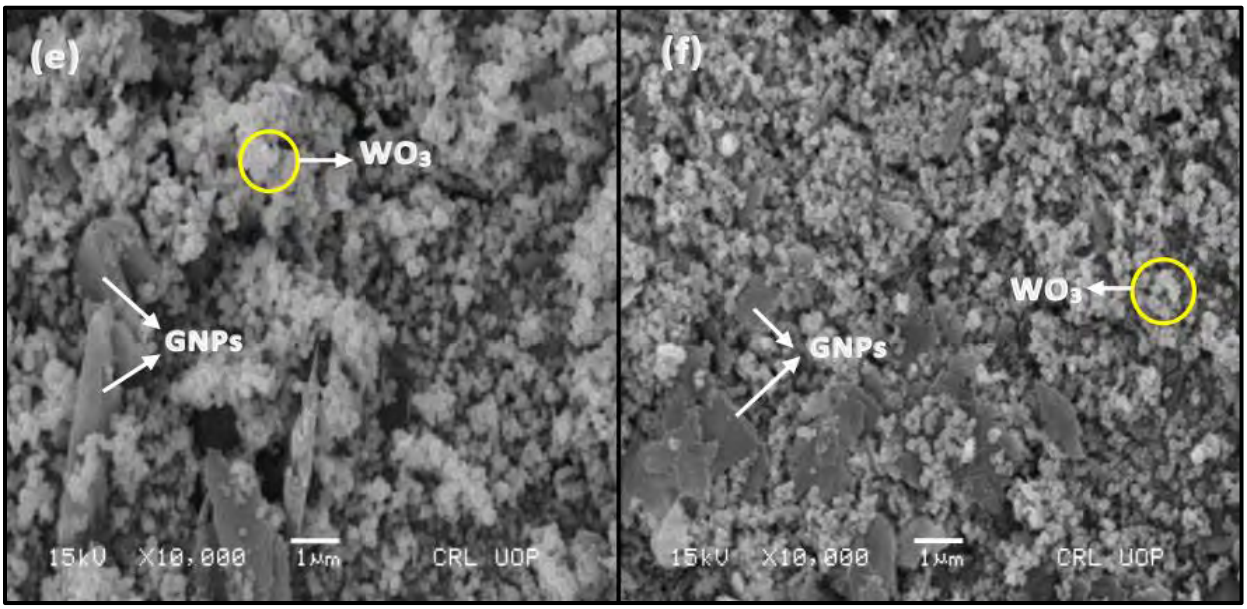

Figure 4.5 SEM images of **(e)** (FexW1-xO3)0.5(GNPs)0.5{x= 5} and (f) (FexW1-xO3)0.5(GNPs)0.5{x= 7} nanocomposites.

Figure 4.5 (e-f) confirms the multiphase nature of the $(Fe_xW_{1-x}O_3)_{0.5}(GNPs)_{0.5}${x= 5 & 7} nanocomposites. SEM images reveal that Fe doped WO_3 nanoparticles reside on the surface of GNPs and hence demonstrate the formation of nanocomposites.

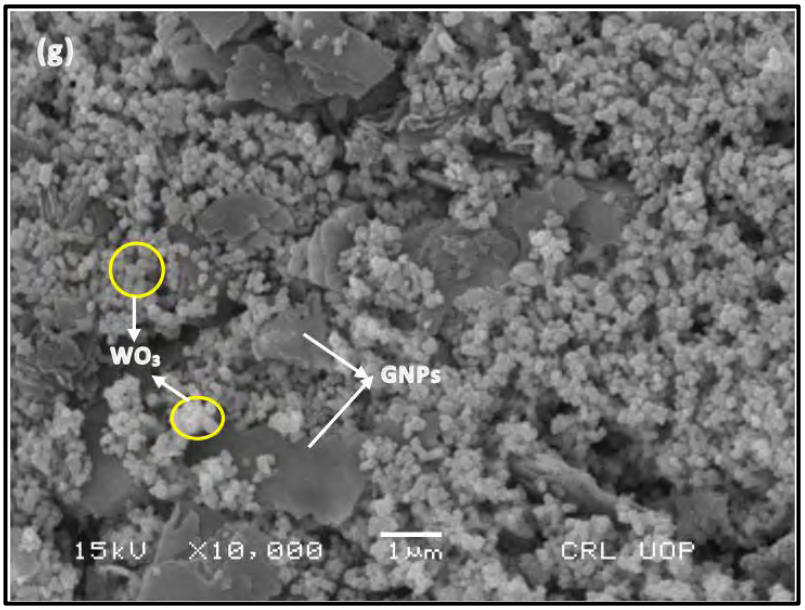

Figure 4.6 (g) SEM image for (FexW1-xO3)0.5(GNPs)0.5{x= 10} nanocomposites.

Figure 4.6 (g) represents the microstructure of $(Fe_xW_{1-x}O_3)_{0.5}(GNPs)_{0.5}${x= 10} nanocomposites. 10 % Fe doped WO_3 nanoparticles seem to be embedded on the surface of GNPs. The assembly again confirms the multiphase nature of the nanocomposites.

4.3 Investigations of Stretching and Bending Modes Analysis

Due to the high surface reactivity, the information about surface chemistry of nanostructures is extremely desirable. To investigate the stretching and bending modes, the surface chemistry and bond formation for the as-prepared samples, the FTIR spectroscopy has been used to obtain data from 500 cm^{-1} to 4000 cm^{-1} range. The bending modes for hydroxyl groups (O-H) has been observed from 1415-1628 cm^{-1} range of wavenumbers. WO_3 nanoparticles possess bands between 500-1000 cm^{-1} range. The stretching modes of O-W-O can be seen at the wavenumber range of 780 cm^{-1}. The FTIR spectra for $(Fe_xW_{1-x}O_3)_{0.5}(GNPs)_{0.5}${x= 0, 3, 5, 7 & 10} nanocomposites are shown if figure 4.7.

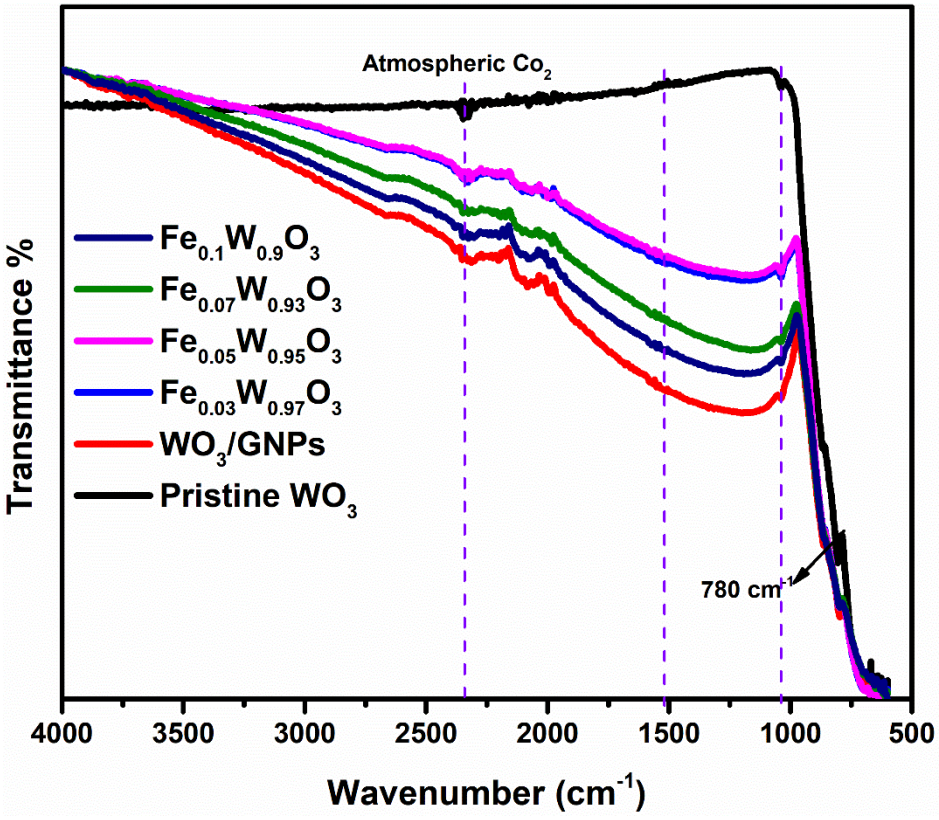

Figure 4.7 FTIR spectra for (FexW1-xO3)0.5(GNPs)0.5{x= 0, 3, 5, 7 & 10} nanocomposites.

The Fe doped WO_3/GNPs and undoped WO_3/GNPs with 50 % GNPs show a minor shift in the 780 cm^{-1} band toward higher wavenumbers. The modes related to Fe_2O_3 has been not confirmed from the FTIR spectra, that suggests, that Fe ions doped successfully in WO_3 monoclinic structures. Peaks shift occurs due to the amalgamation of GNPs matrix in the nanocomposites. FTIR results, therefore, confirm the formation of nanocomposites and corroborate with XRD results [67].

4.4 Optical Characteristics Investigations

To know about the optical properties of $(Fe_xW_{1-x}O_3)_{0.5}(GNPs)_{0.5}$ {x= 0, 3, 5, 7 & 10} nanocomposites, the diffuse reflectance spectroscopy has been performed using photo

spectrometer at room temperature from 200 nm to 1200 nm wavelength range. Figure 4.8 displays the DRS spectra for the all the samples. Undoped WO_3 has a strong absorption in the ultraviolet region. While in-corporation of GNPs with WO_3 nanocomposites the curve revealed absorption values without spectra region. This is due to the full coverage of WO_3 nanoparticles on the surface of GNPs.

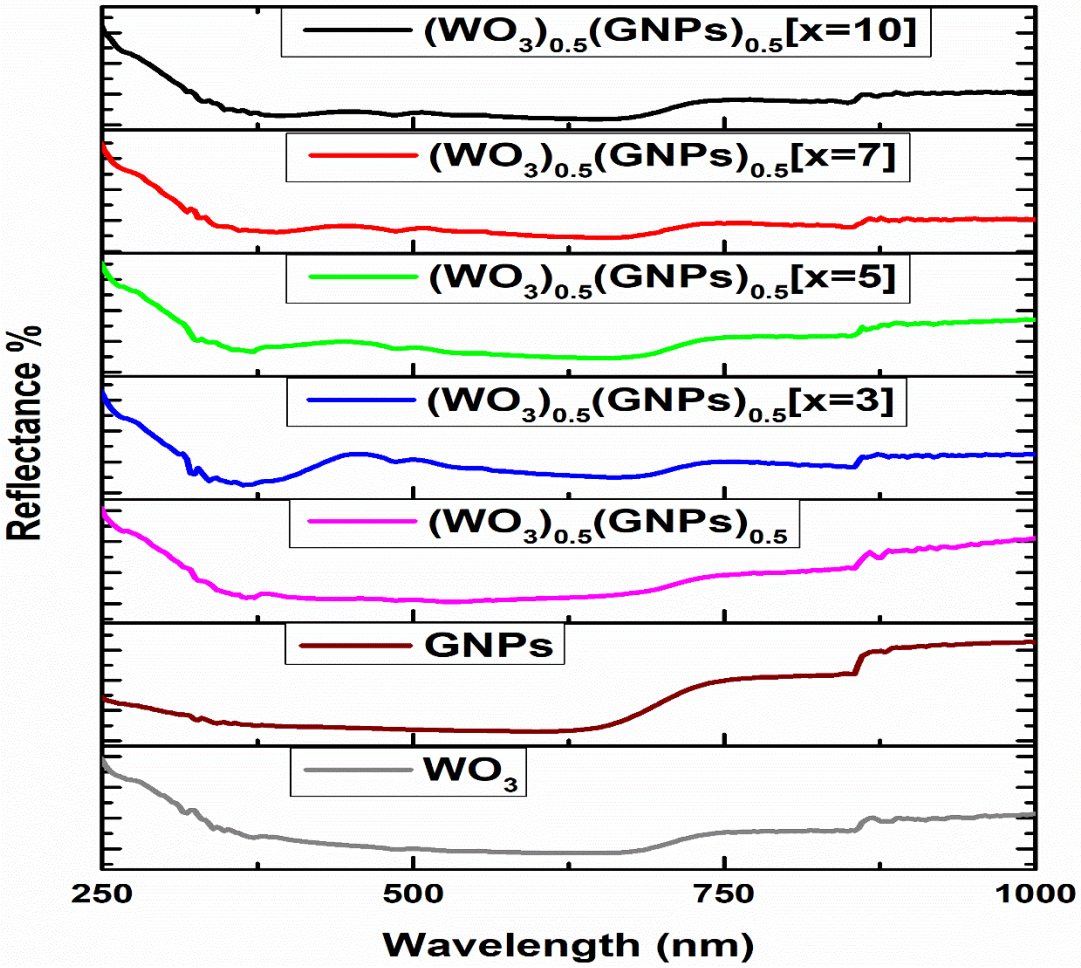

Figure 4.8 UV-visible plot for (FexW1-xO3)0.5(GNPs)0.5{x= 0, 3, 5, 7 & 10} nanocomposites.

The percentage reflectance spectra of WO_3 and (3, 5, 7 and 10 %)Fe doped WO_3/GNPs nanocomposites have been recorded in the wavelength range (250-1200 nm) as shown in figure

4.8. The optical band gap is calculated by extrapolating tangent to the square of absorbance time energy along y-axis and energy along x-axis as shown in figure 4.9.

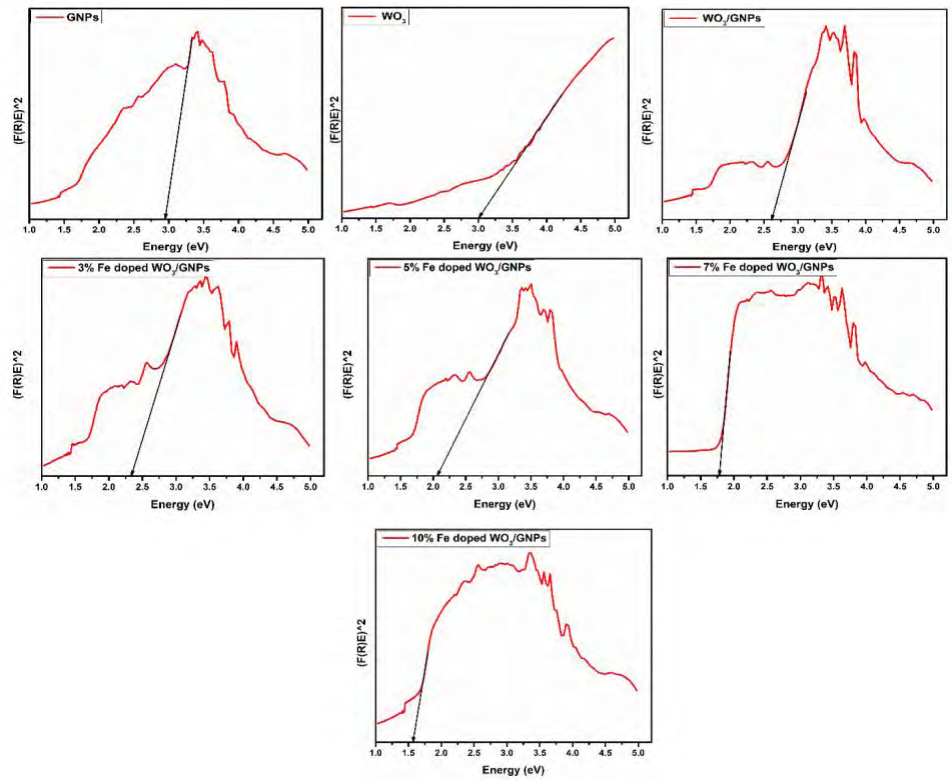

Figure 4.9 Bandgaps of (FexW1-xO3)0.5(GNPs)0.5{x= 0, 3, 5, 7 & 10} nanocomposites.

The calculated indirect optical band gap of monoclinic crystalline WO_3 nanoparticles is in well agreement with the early reported values and is shown in table 4.3. Interestingly, the decrease in the optical band gap is observed with the increase in the Fe doping into WO_3 nanoparticles.

Table 4.3 Bandgap for $(Fe_xW_{1-x}O_3)_{0.5}(GNPs)_{0.5}\{x= 0, 3, 5, 7 \& 10\}$ nanocomposites.

S. No.	Sample	Bandgap (eV)
1	WO_3	3.0
2	GNPs	2.8
3	$(Fe_xW_{1-x}O_3)_{0.5}(GNPs)_{0.5}$	2.7
4	$(Fe_xW_{1-x}O_3)_{0.5}(GNPs)_{0.5}\{x= 3\}$	2.3
5	$(Fe_xW_{1-x}O_3)_{0.5}(GNPs)_{0.5}\{x= 5\}$	2.3
6	$(Fe_xW_{1-x}O_3)_{0.5}(GNPs)_{0.5}\{x= 7\}$	1.6
7	$(Fe_xW_{1-x}O_3)_{0.5}(GNPs)_{0.5}\{x= 10\}$	1.6

This decrease in the band gap may be attributed to some intermediate energy levels formed between conduction band and valence band of WO_3. Moreover, larger ionic radius dopant increases lattice parameters which causes decrease in the density of atoms [68]. In such systems, the valence electrons are not tightly bounded, small energy is required to excite which causes decrease in the band gap. In the tuning of optical band gap via doping, there are many factors which influence the band gap such as quantum confinement effect, lattice strain present in the host matrix, structural disorder, impurities present at grain boundaries and band bending effect.

4.5 UV Light Driven Degradation of Methyl Blue

UV light driven photocatalytic activity has been performed for $(Fe_xW_{1-x}O_3)_{0.5}(GNPs)_{0.5}\{x= 0, 3, 5, 7 \& 10\}$ nanocomposites, to observe their degradation ability against methylene blue (MB). The degradation spectra for $(Fe_xW_{1-x}O_3)_{0.5}(GNPs)_{0.5}\{x= 0, 3, 5, 7 \& 10\}$ nanocomposites are shown in figure 4.10 to figure 4.17.

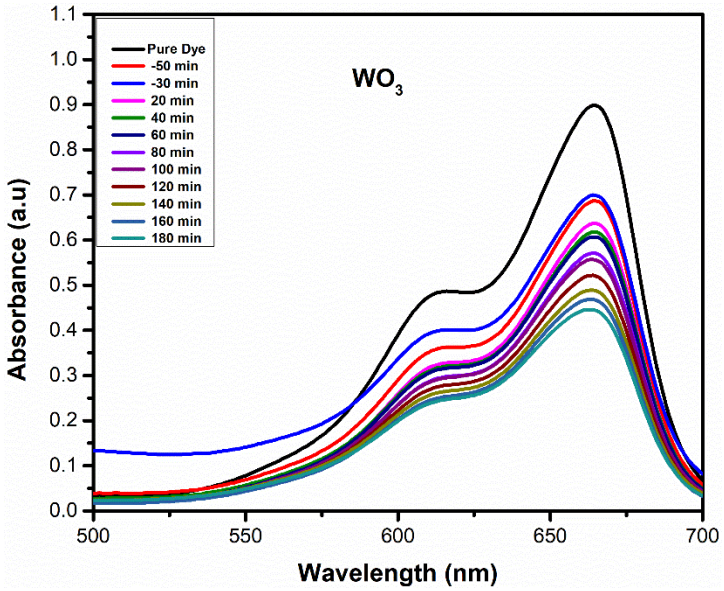

Figure 4.10 Degradation of methyl blue(MB) by undoped WO3 nanoparticles.

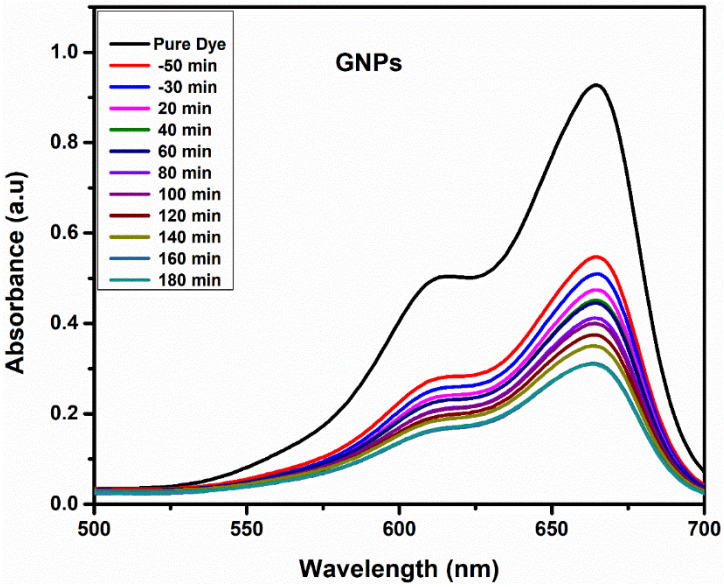

Figure 4.11 Degradation of MB by graphene nanoplatelets (GNPs).

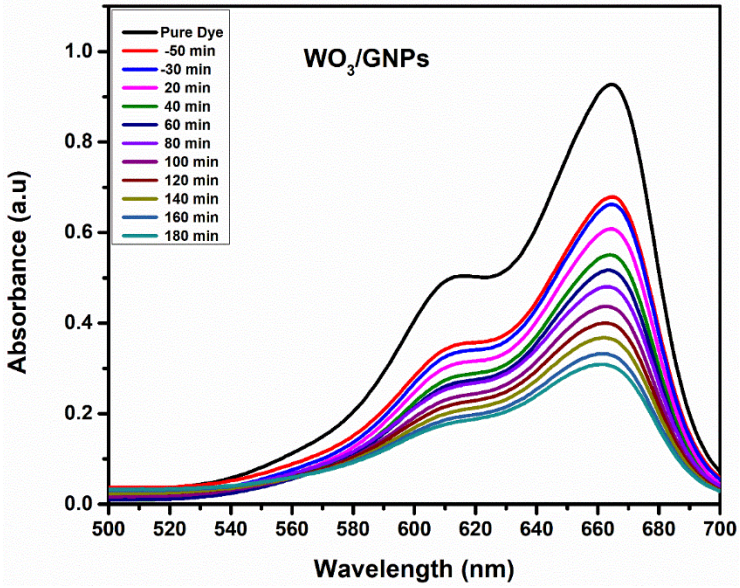

Figure 4.12 Degradation of MB by (WO3)0.5(GNPs)0.5 nanocomposites.

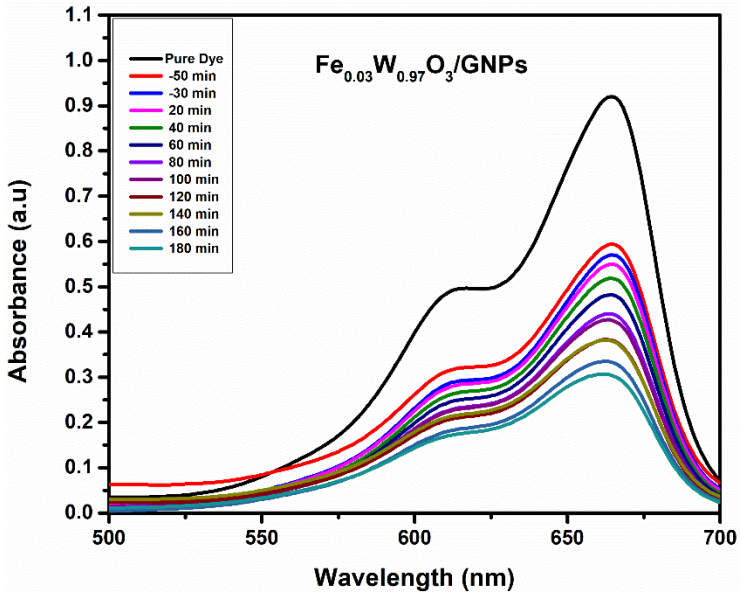

Figure 4.13 Degradation of MB by (FexW1-xO3)0.5(GNPs)0.5{x= 3} nanocomposites.

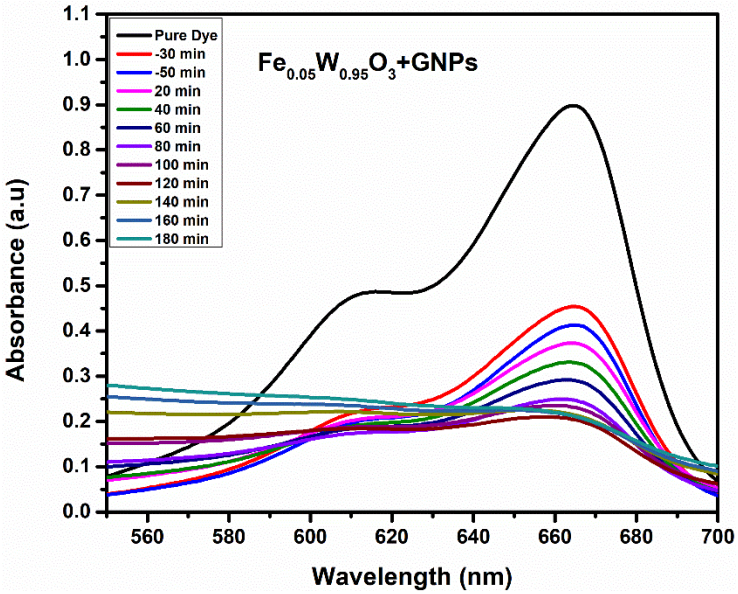

Figure 4.14 Degradation of MB by (FexW1-xO3)0.5(GNPs)0.5{x= 5} nanocomposites.

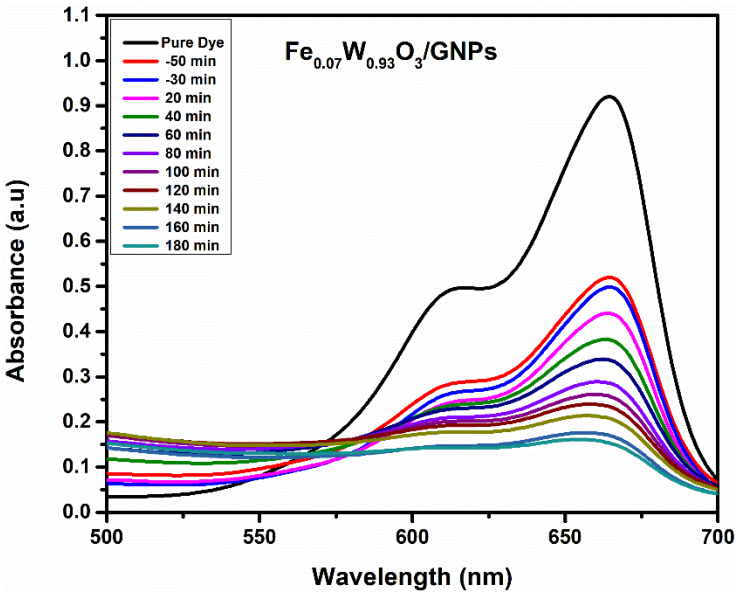

Figure 4.15 Degradation of MB by (FexW1-xO3)0.5(GNPs)0.5{x= 7} nanocomposites.

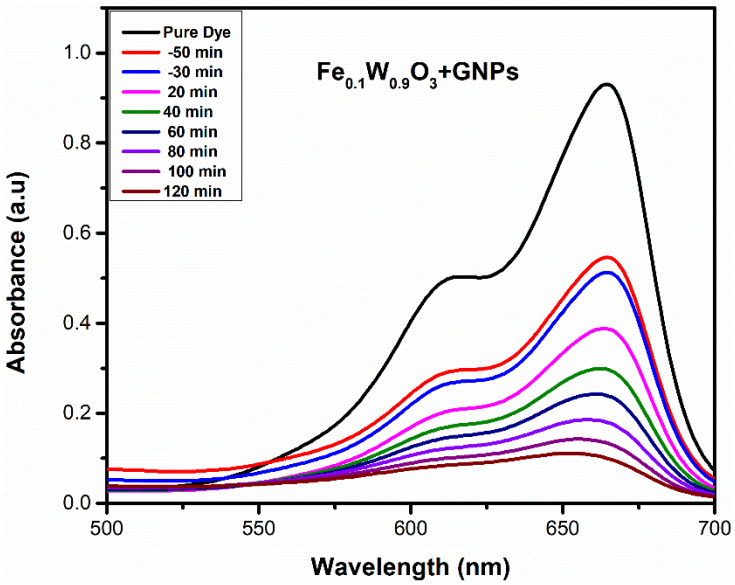

Figure 4.16 Photodegradation of (FexW1-xO3)0.5(GNPs)0.5{x= 10} nanocomposites.

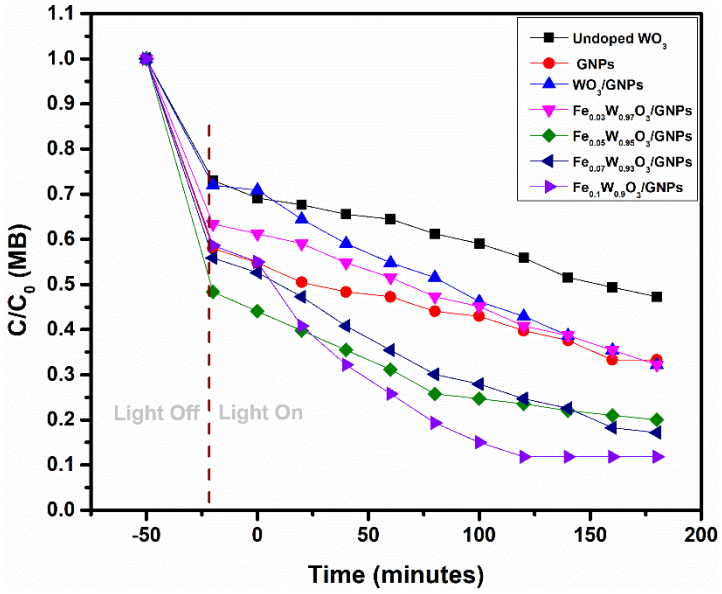

Figure 4.17 Photocatalytic degradation of (FexW1-xO3)0.5(GNPs)0.5{x= 0, 3, 5, 7 & 10} nanocomposites.

In order to represent the degradation of MB, the change in concentration with respect to time is plotted. The degradation profile of MB in presence of $(Fe_xW_{1-x}O_3)_{0.5}(GNPs)_{0.5}${x= 0, 3, 5, 7 & 10} nanocomposites is shown in figure 4.17. The degradation percentage is plotted against

time [69]. The data reveals that the degradation percentage of MB increases from undoped WO_3 to $(Fe_xW_{1-x}O_3)_{0.5}(GNPs)_{0.5}\{x= 10\}$ nanocomposites.

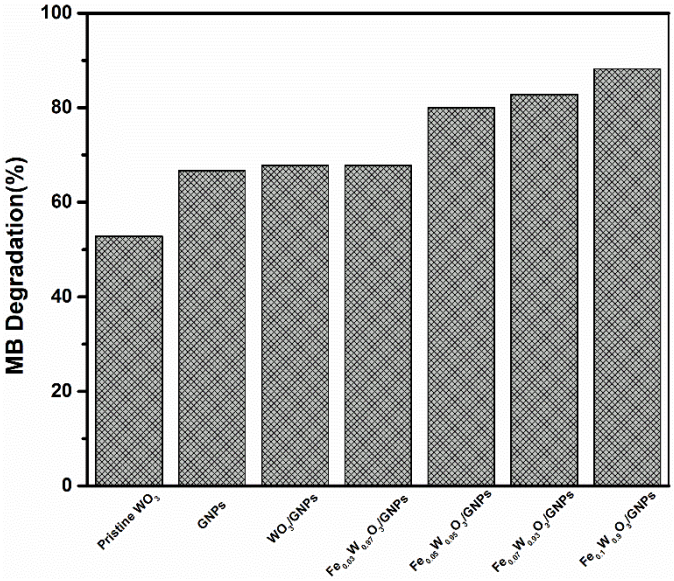

Figure 4.18 Degradation percentage of MB by (FexW1-xO3)0.5(GNPs)0.5{x= 0, 3, 5, 7 & 10} nanocomposites.

Percentage degradation for $(Fe_xW_{1-x}O_3)_{0.5}(GNPs)_{0.5}\{x= 0, 3, 5, 7 \& 10\}$ nanocomposites have been shown in figure 4.18. For 10 % Fe doped WO_3/GNPs, 88 % degradation has been noted under UV light irradiation in three hours. To calculate the rate constant of the reaction, the number $\ln \frac{C}{C_o}$ is plotted against time *t* using linear curve fitting. The rate constant of the reaction is determined by the given equation;

$$\ln\left(\frac{C_o}{C}\right) = kt \tag{4.1}$$

In the above equation C_o and C denote the early and last concentration of the sample taken for UV scan while *k* denotes the rate constant respectively. Different values of *k* have been calculated using equation 4.1 for $(Fe_xW_{1-x}O_3)_{0.5}(GNPs)_{0.5}\{x= 0, 3, 5, 7 \& 10\}$ nanocomposites are

0.00262 min^{-1}, 0.00372 min^{-1}, 0.00446 min^{-1}, 0.00405 min^{-1}, 0.00589 min^{-1}, 0.00689 min^{-1}, 0.00989 min^{-1} respectively.

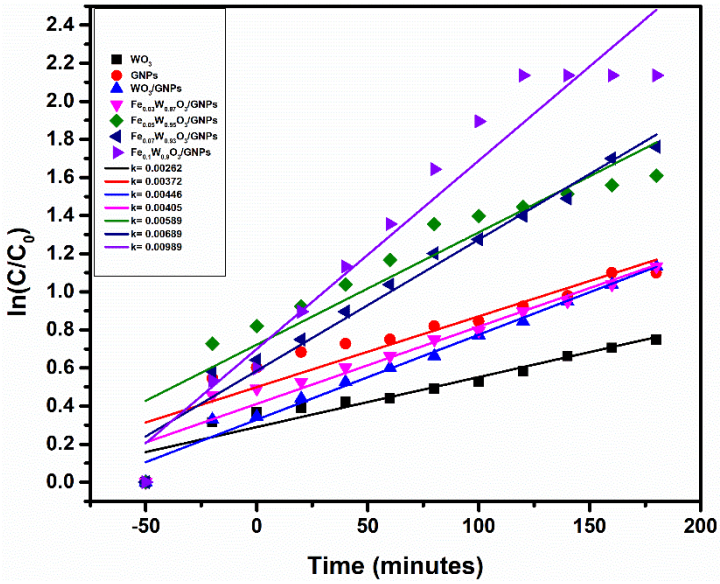

Figure 4.19 Photocatalytic degradation kinetics of MB by (FexW1-xO3)0.5(GNPs)0.5{x= 0, 3, 5, 7 & 10} nanocomposites.

It has been concluded that the rate of the reaction increases pointedly with the Fe dopant concentration. The highest *k* value has been noted for $(Fe_xW_{1-x}O_3)_{0.5}(GNPs)_{0.5}${x= 3} nanocomposites that is 0.00989 min^{-1}. The best activity of this photocatalyst that degrade MB up to 88 % is due to the proper quantity of Fe as dopant and GNPs concentration. Photocatalytic degradation kinetics for $(Fe_xW_{1-x}O_3)_{0.5}(GNPs)_{0.5}${x= 0, 3, 5, 7 & 10} nanocomposites is shown in figure 4.19.

The general mechanism for photocatalysis is shown in Figure 4.20. The purpose for the addition of GNPs in WO_3 is to increase the surface area that encourages the maximum MB during adsorption. As UV light is exposed on these nanocomposites, the electrons in WO_3 nanoparticles get excited to conduction band. Since GNPs has good conductivity, therefore the

electrons excited from WO_3 nanoparticles are easily taken by the sheets of GNPs. High value of conductivity for GNPs offer a leading network and minimize the rate for the recombination of electron-hole pairs in WO_3 nanoparticles. Reactive oxygen species are created because of charge carriers. These oxygen species play an important role in photocatalysis and hence change the chemical structure of MB. The end products in photocatalysis are water and carbon dioxide. Enhanced photocatalytic activity of $(Fe_xW_{1-x}O_3)_{0.5}(GNPs)_{0.5}\{x= 3\}$ nanocomposites are the result of conductive nature of GNPs, increased surface area and lowest band gap. The chemical reaction that occur at the surface of nanocomposites are pictorially represented below,

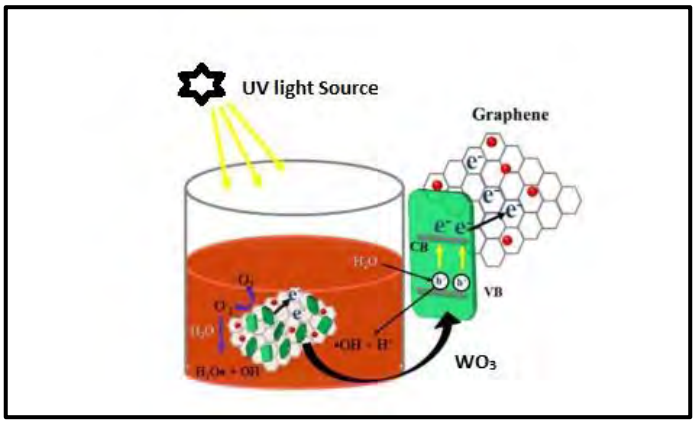

Figure 4.20 Schematic representation of chemical reaction of MB at the surface of nanocomposites [70].

It is notable that WO_3 nanoparticles display very low photocatalytic activity due to following proofs. Excited electrons tend to de-excite quickly into the valence band. Electronic trap in the form of graphene is not available in this case. Only a few electrons can get stuck in defect states of WO_3. This makes electrons and holes inaccessible for generation of appropriate number of reactive oxygen species [71]. Other factors that accounts for low photodegradation performance of WO_3 are its comparatively higher bandgap energy and low surface area. A higher optical bandgap energy of WO_3 is responsible for slower photoexcitation. A low surface area

results in less adsorption of methyl orange during the process. Subsequently, neat WO_3 gives much lower photodegradation efficiency.

4.6 Antibacterial Activity

Graphene based materials are planned for decontamination of water from pathogenic microbes. Antibacterial performance of these nanomaterials may depend on various factors like morphology, ability to produce reactive oxygen species, conductivity and their composition. Considering these factors, we predict to design a bactericidal nanomaterial (Fe doped WO_3 and graphene) with an aim to utilize the antibacterial features of both WO_3 and graphene in a combined fashion for bacterial growth inhibition.

In order to study the influence of WO_3/GNPs nanocomposites on growth inhibition of Gram positive and Gram-negative bacteria, we have assessed antibacterial properties of a series of nanocomposites with different Fe content. The zone of inhibitions of bacteria for WO_3 and its nanocomposites with graphene are presented in Figure 4.21(a)- (b).

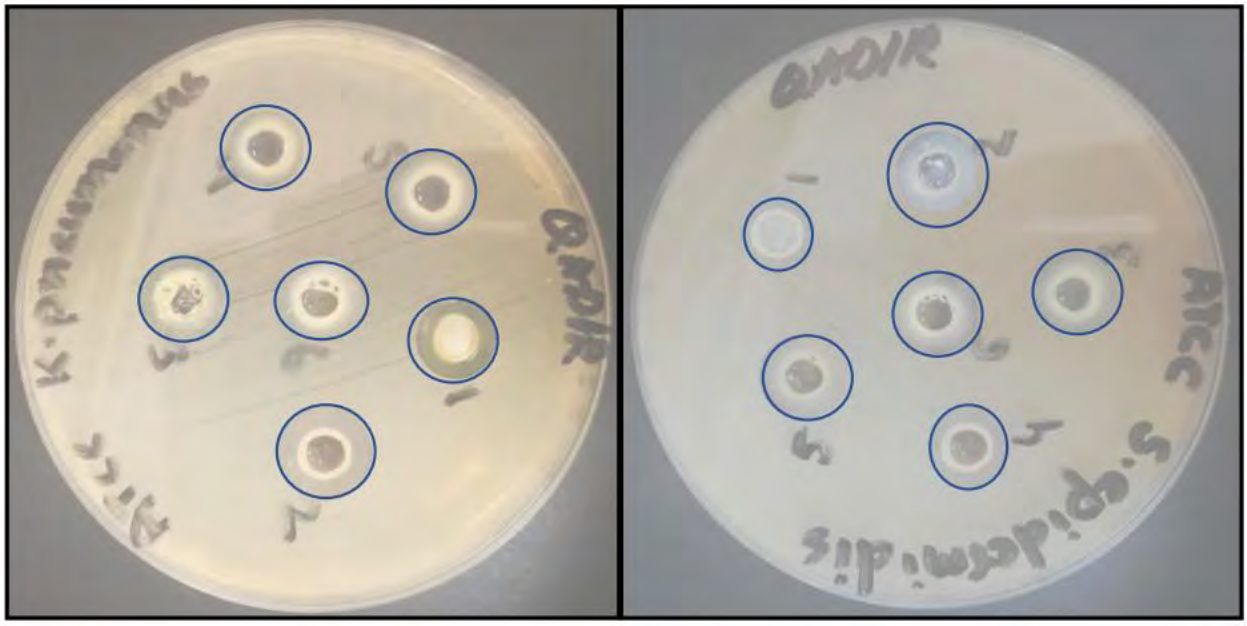

Figure 4.21 (a) k. pneumoniae antibacterial activity against (FexW1-xO3)0.5(GNPs)0.5{x= 0, 3, 5, 7 & 10} nanocomposites. **(b)** S. epidermidis antibacterial activity for (FexW1-xO3)0.5(GNPs)0.5{x= 0, 3, 5, 7 & 10} nanocomposites.

Gram negative bacteria (*Klebsiella pneumoniae*) is found more susceptible than gram positive bacteria i.e. *Staphylococcus epidermidis*. WO_3-GNPs demonstrate highest activity against *Klebsiella pneumoniae* with ZOIs i.e. 12 mm followed by 10 % Fe doped WO_3-GNPs (11 mm). Least activity has been observed against pure 10 mm WO_3. Table 4.4 shows antibacterial activity of the tested NPs and nanocomposites samples. Moreover, *Staphylococcus epidermidis* demonstrated highest susceptibility against WO_3-GNPs (ZOI, 11 mm) that is previously well reported, while pure WO_3-NPs exhibited less activity than 50 % WO_3-GNPs nanocomposites i.e. 9 mm. 10 % Fe doped exhibited highest activity (12 mm) among the doped Fe-WO_3 nanocomposites, while 3 % Fe doped showed less activity against subjected gram-positive bacteria i.e. 9 mm.

Table 4.4 Zone of inhibitions in diameter for different samples.

S. No	Sample Name	*Klebsiella pneumoniae*	*Staphylococcus epidermidis*
1	WO_3	10 mm	9 mm
2	$(WO_3)_{0.5}(GNPs)_{0.5}$	12 mm	11 mm
3	$(Fe_xW_{1-x}O_3)_{0.5}(GNPs)_{0.5}$ {x= 3}	11 mm	9 mm
4	$(Fe_xW_{1-x}O_3)_{0.5}(GNPs)_{0.5}$ {x= 5}	10.5 mm	9.5 mm
5	$(Fe_xW_{1-x}O_3)_{0.5}(GNPs)_{0.5}$ {x= 7}	11 mm	10 mm
6	$(Fe_xW_{1-x}O_3)_{0.5}(GNPs)_{0.5}$ {x= 10}	11. 5 mm	12 mm

Table 4.4 shows the zone of inhibitions for $(Fe_xW_{1-x}O_3)_{0.5}(GNPs)_{0.5}$ {x= 0, 3, 5, 7 & 10} nanocomposites. The highest zone of inhibitions has been noted for $(Fe_xW_{1-x}O_3)_{0.5}(GNPs)_{0.5}$ {x= 10} nanocomposites for *Staphylococcus epidermidis* (Gram positive bacteria) and *Klebsiella pneumoniae* (Gram negative bacteria) shows highest ZOIs for WO_3/GNPs nanocomposites.

The exact mechanism of antibacterial properties of graphene nanocomposite is debatable and not yet well-known [72]. Several mechanisms have been proposed that account for toxicity of graphene or its nanocomposites. Here, we briefly give a summary of probable mechanisms. For metal oxides and graphene nanocomposites, it is proposed that damage of proteins caused by either metal oxides alone or metal oxides/graphene combinedly leads to bacterial inactivity [73]. In our case, the first mechanism asserts that membrane rupture results the cell death when graphene sheets encounter bacterial surface. The edges of graphene act as sharp scissors. However, it was established that the membrane distraction is dependent on size of graphene sheets. Membranes disintegration can also be followed by internalization of nanostructures, which causes damage to bacteria. The wrapping of wrinkled sheets is another reason that can isolate bacteria from nutrients and it proves to be lethal for them [74]. In addition, metal oxides

are also known to damage the cell membranes and so their composites with graphene. It has been proposed that the release of metal ions by metal oxide results the increase localized concentration, which may cause fighting on bacterial surface, with subsequent leakage of cytoplasmic content from cell. Intimate contact between graphene sheets and metal ions synergistically encourage bacterial apoptosis. Many of recent experiments validate generation of reactive oxygen species which may be the consequence of mechanisms. However, it is suggested in another work that graphene establishes conductivity dependent cytotoxicity. The charge transfer between graphene and bacterial membranes leads to charge imbalance on bacterial surface with subsequent generation of reactive oxygen species [43]. The induced oxidative stress leads to bacterial apoptosis.

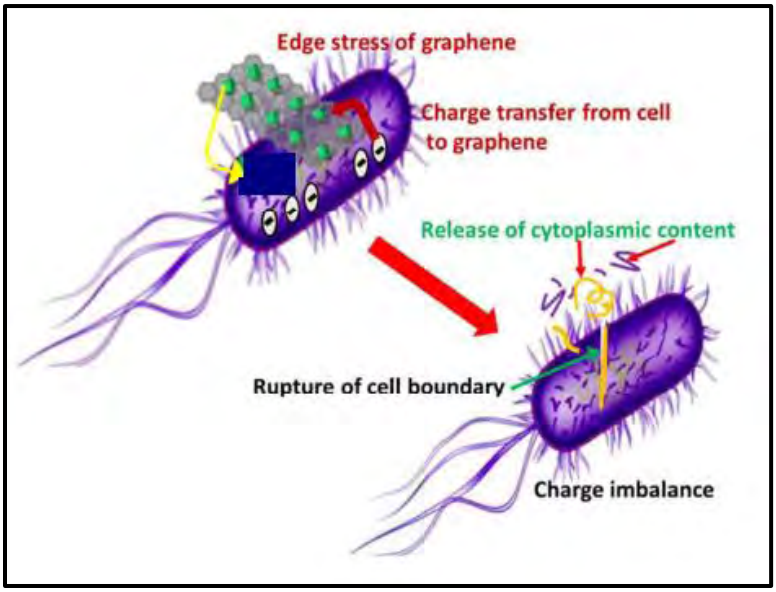

Figure 4.22 General mechanism of antibacterial activity [70].

In the light of discussion presented above, we believe that synergistic effect created by edge stress of graphene and protein impairment leads to bactericidal activity observed in our

findings. A graphic layout describes the various possible ways to destruct cell in figure 4.22. The nanocomposite prepared with definite composition of graphene i.e. $(Fe_xW_{1-x}O_3)_{0.5}(GNPs)_{0.5}\{x= 10\}$ nanocomposites has shown high growth inhibition of both Gram positive and Gram-negative bacteria during incubation time. Our experimental findings distinguish $(Fe_xW_{1-x}O_3)_{0.5}(GNPs)_{0.5}$ $\{x= 10\}$ nanocomposites as a novel nanomaterial for complete pathogenic control.

Conclusions

In conclusion, $(Fe_xW_{1-x}O_3)_{0.5}(GNPs)_{0.5}${x= 0, 3, 5, 7 & 10} nanocomposites have been prepared using ex-situ facile chemical co-precipitation method. Structural investigation illustrates the monoclinic structure of WO_3 nanoparticles, and slight shift in prominent peaks towards lower angle affirms the effective doping of Fe into WO_3. In XRD pattern of nanocomposites, the presence of characteristics peak related to graphene provides evidence of the formation of $(Fe_xW_{1-x}O_3)_{0.5}(GNPs)_{0.5}${x= 0, 3, 5, 7 & 10} nanocomposites in which both phases are coexistent without impurity phase of iron oxide etc. SEM images depict the spherical morphology of WO_3 and nanoplates like morphology of GNPs. The nanocomposite images demonstrate that the spherical nanoparticles of WO_3 have been dispersed over GNPs sheets. The vibrational analysis confirms the presence of stretching mode of W-O-W and characteristic mode of GNPs. The focus of this research is to tune the optical band gap of WO_3 by Fe doping. The increase in Fe doping decreases the optical band gap due to generation of impurity state between valance and conduction band. This decrease in optical band gap is beneficial to enhance the photocatalytic activity. Moreover, the GNPs and Fe doping produce crystal defects and during excitation from valance band to conduction band the electron trapped in these defects and decrease the electron-hole recombination rates and hence speed up the degradation process, which has been observed in this research. The $(Fe_xW_{1-x}O_3)_{0.5}(GNPs)_{0.5}${x= 0, 3, 5, 7 & 10} nanocomposite also shows toxic nature toward the pathogenic bacteria. Hence this prepared multifunctional $(Fe_xW_{1-x}O_3)_{0.5}(GNPs)_{0.5}${x= 0, 3, 5, 7 & 10} nanocomposites can be used as antibacterial agent as well as photocatalysts for cleaning of wastewater.

References

1. Pokropivny, V. and V. Skorokhod, *Classification of nanostructures by dimensionality and concept of surface forms engineering in nanomaterial science.* Materials Science and Engineering: C, 2007. **27**(5-8): p. 990-993.
2. Roco, M.C. and W.S. Bainbridge, *Societal implications of nanoscience and nanotechnology: Maximizing human benefit.* Journal of Nanoparticle Research, 2005. **7**(1): p. 1-13.
3. Feynman, R.P., *There's plenty of room at the bottom.* Engineering and science, 1960. **23**(5): p. 22-36.
4. Fang, M., et al., *Degradation of nanoRNA is performed by multiple redundant RNases in Bacillus subtilis.* Nucleic acids research, 2009. **37**(15): p. 5114-5125.
5. Tiwari, J.N., R.N. Tiwari, and K.S. Kim, *Zero-dimensional, one-dimensional, two-dimensional and three-dimensional nanostructured materials for advanced electrochemical energy devices.* Progress in Materials Science, 2012. **57**(4): p. 724-803.
6. Rotello, V.M., *Nanoparticles: building blocks for nanotechnology*. 2004: Springer Science & Business Media.
7. Kelsall, R., I.W. Hamley, and M. Geoghegan, *Nanoscale science and technology*. 2005: John Wiley & Sons.
8. Gleiter, H., *Nanostructured materials.* Advanced Materials, 1992. **4**(7-8): p. 474-481.
9. Ozin, G.A., *Nanochemistry: synthesis in diminishing dimensions.* Advanced Materials, 1992. **4**(10): p. 612-649.
10. Rittner, M.N. and T. Abraham, *The nanostructured materials industry.* American Ceramic Society Bulletin, 1997. **76**(6): p. 51-53.
11. Verweij, H., *Nanocrystalline and nanoporous ceramics.* Advanced materials, 1998. **10**(17): p. 1483-1486.
12. Simon, U., *Charge transport in nanoparticle arrangements.* Advanced Materials, 1998. **10**(17): p. 1487-1492.
13. Himpsel, F., et al., *Magnetic nanostructures.* Advances in physics, 1998. **47**(4): p. 511-597.
14. McHenry, M.E., M.A. Willard, and D.E. Laughlin, *Amorphous and nanocrystalline materials for applications as soft magnets.* Progress in Materials Science, 1999. **44**(4): p. 291-433.
15. Moriarty, P., *Nanostructured materials.* Reports on Progress in Physics, 2001. **64**(3): p. 297.
16. Cohen, M.L., *Nanotubes, nanoscience, and nanotechnology.* Materials Science and Engineering: C, 2001. **15**(1-2): p. 1-11.
17. Kelly, K.L., et al., *The optical properties of metal nanoparticles: the influence of size, shape, and dielectric environment*. 2003, ACS Publications.
18. Raj, K. and R. Moskowitz, *Commercial applications of ferrofluids.* Journal of Magnetism and Magnetic Materials, 1990. **85**(1-3): p. 233-245.
19. Rice, P. and J. Moreland, *A new look at the Bitter method of magnetic imaging.* Review of scientific instruments, 1991. **62**(3): p. 844-845.
20. Pankhurst, Q. and R. Pollard, *Fine-particle magnetic oxides.* Journal of Physics: Condensed Matter, 1993. **5**(45): p. 8487.
21. Shafi, K.V., A. Gedanken, and R. Prozorov, *Surfactant-Assisted Self-Organization of Cobalt Nanoparticles in a Magnetic Fluid.* Advanced Materials, 1998. **10**(8): p. 590-593.
22. Toneguzzo, P., et al., *Monodisperse ferromagnetic particles for microwave applications.* Advanced Materials, 1998. **10**(13): p. 1032-1035.

23. Toshima, N. and T. Yonezawa, *Bimetallic nanoparticles—novel materials for chemical and physical applications.* New Journal of Chemistry, 1998. **22**(11): p. 1179-1201.
24. Chen, S., et al., *Gold nanoelectrodes of varied size: transition to molecule-like charging.* Science, 1998. **280**(5372): p. 2098-2101.
25. Shipway, A.N., E. Katz, and I. Willner, *Nanoparticle arrays on surfaces for electronic, optical, and sensor applications.* ChemPhysChem, 2000. **1**(1): p. 18-52.
26. Gomez-Romero, P., *Hybrid organic–inorganic materials—in search of synergic activity.* Advanced Materials, 2001. **13**(3): p. 163-174.
27. Kamat, P.V., *Photophysical, photochemical and photocatalytic aspects of metal nanoparticles*. 2002, ACS Publications.
28. Brigger, I., C. Dubernet, and P. Couvreur, *Nanoparticles in cancer therapy and diagnosis.* Advanced drug delivery reviews, 2012. **64**: p. 24-36.
29. Daniel, M.-C. and D. Astruc, *Gold nanoparticles: assembly, supramolecular chemistry, quantum-size-related properties, and applications toward biology, catalysis, and nanotechnology.* Chemical reviews, 2004. **104**(1): p. 293-346.
30. Wang, D. and H. Möhwald, *Template-directed colloidal self-assembly–the route to 'top-down'nanochemical engineering.* Journal of Materials Chemistry, 2004. **14**(4): p. 459-468.
31. Matsui, K., T. Kyotani, and A. Tomita, *Hydrothermal Synthesis of Single-Crystal Ni (OH) 2 Nanorods in a Carbon-Coated Anodic Alumina Film.* Advanced Materials, 2002. **14**(17): p. 1216-1219.
32. Ito, A., et al., *Medical application of functionalized magnetic nanoparticles.* Journal of bioscience and bioengineering, 2005. **100**(1): p. 1-11.
33. Jain, P. and T. Pradeep, *Potential of silver nanoparticle-coated polyurethane foam as an antibacterial water filter.* Biotechnology and bioengineering, 2005. **90**(1): p. 59-63.
34. Kralik, M. and A. Biffis, *Catalysis by metal nanoparticles supported on functional organic polymers.* Journal of Molecular Catalysis A: Chemical, 2001. **177**(1): p. 113-138.
35. Stone, V., et al., *Nanomaterials for environmental studies: classification, reference material issues, and strategies for physico-chemical characterisation.* Science of the total environment, 2010. **408**(7): p. 1745-1754.
36. Lue, J.T., *Physical properties of nanomaterials.* Encyclopedia of nanoscience and nanotechnology, 2007. **10**(1): p. 1-46.
37. Ray, P.C., *Size and shape dependent second order nonlinear optical properties of nanomaterials and their application in biological and chemical sensing.* Chemical reviews, 2010. **110**(9): p. 5332-5365.
38. Li, J. and J.Z. Zhang, *Optical properties and applications of hybrid semiconductor nanomaterials.* Coordination Chemistry Reviews, 2009. **253**(23-24): p. 3015-3041.
39. Fasol, G., *Room-temperature blue gallium nitride laser diode.* Science, 1996. **272**(5269): p. 1751-1752.
40. Someya, T., et al., *Room temperature lasing at blue wavelengths in gallium nitride microcavities.* Science, 1999. **285**(5435): p. 1905-1906.
41. Reddy, K.M., S.V. Manorama, and A.R. Reddy, *Bandgap studies on anatase titanium dioxide nanoparticles.* Materials Chemistry and Physics, 2003. **78**(1): p. 239-245.
42. Law, M., J. Goldberger, and P. Yang, *Semiconductor nanowires and nanotubes.* Annu. Rev. Mater. Res., 2004. **34**: p. 83-122.
43. Li, J., et al., *Antibacterial activity of large-area monolayer graphene film manipulated by charge transfer.* Scientific reports, 2014. **4**: p. 4359.

44. Puzder, A., et al., *Structural stability and optical properties of nanomaterials with reconstructed surfaces.* Physical review letters, 2003. **91**(15): p. 157405.
45. Ovais, M., et al., *Current state and prospects of the phytosynthesized colloidal gold nanoparticles and their applications in cancer theranostics.* Applied microbiology and biotechnology, 2017. **101**(9): p. 3551-3565.
46. Yurkov, G.Y., et al., *Electrical and magnetic properties of nanomaterials containing iron or cobalt nanoparticles.* Inorganic Materials, 2007. **43**(8): p. 834-844.
47. Fecht, H.-J., *Mechanical properties of nanomaterials.*
48. Qin, J., et al., *Graphene-wrapped WO 3 nanoparticles with improved performances in electrical conductivity and gas sensing properties.* Journal of Materials Chemistry, 2011. **21**(43): p. 17167-17174.
49. Weil, M. and W.-D. Schubert, *The Beautiful Colours of Tungsten Oxides.* Newsletter, 2013.
50. Zhu, K., et al., *Crystalline WO3 nanowires synthesized by templating method.* Chemical Physics Letters, 2003. **377**(3-4): p. 317-321.
51. Woodward, P., A. Sleight, and T. Vogt, *Ferroelectric tungsten trioxide.* Journal of Solid State Chemistry, 1997. **131**(1): p. 9-17.
52. Li, Y., et al., *Defect engineering of air-treated WO3 and Its enhanced visible-light-driven photocatalytic and electrochemical performance.* The Journal of Physical Chemistry C, 2016. **120**(18): p. 9750-9763.
53. Wang, F., C. Di Valentin, and G. Pacchioni, *Doping of WO3 for photocatalytic water splitting: hints from density functional theory.* The Journal of Physical Chemistry C, 2012. **116**(16): p. 8901-8909.
54. Nair, R.R., et al., *Fine structure constant defines visual transparency of graphene.* Science, 2008. **320**(5881): p. 1308-1308.
55. Gao, W., *The chemistry of graphene oxide*, in *Graphene oxide*. 2015, Springer. p. 61-95.
56. Lee, C., et al., *Measurement of the elastic properties and intrinsic strength of monolayer graphene.* science, 2008. **321**(5887): p. 385-388.
57. Jafri, R.I., N. Rajalakshmi, and S. Ramaprabhu, *Nitrogen doped graphene nanoplatelets as catalyst support for oxygen reduction reaction in proton exchange membrane fuel cell.* Journal of Materials Chemistry, 2010. **20**(34): p. 7114-7117.
58. Koo, J.H., *Polymer nanocomposites*. 2006: McGraw-Hill Professional Pub.
59. Gui, Y., et al., *Synthesis of hemispherical WO3/graphene nanocomposite by a microwave-assisted hydrothermal method and the gas-sensing properties to triethylamine.* Materials Letters, 2015. **155**: p. 4-7.
60. Zhou, M., J. Yan, and P. Cui, *Synthesis and enhanced photocatalytic performance of WO3 nanorods@ graphene nanocomposites.* Materials Letters, 2012. **89**: p. 258-261.
61. Lü, M., et al., *Applications of graphene-based materials in environmental protection and detection.* Chinese Science Bulletin, 2013. **58**(22): p. 2698-2710.
62. Huczko, A., *Template-based synthesis of nanomaterials.* Applied Physics A, 2000. **70**(4): p. 365-376.
63. Warren, B.E., *X-ray Diffraction*. 1969: Courier Corporation.
64. Khursheed, A., *Scanning electron microscope*. 2007, Google Patents.
65. Mehmood, F., et al., *Structural, Raman and photoluminescence properties of Fe doped WO3 nanoplates with anti cancer and visible light driven photocatalytic activities.* Journal of Alloys and Compounds, 2017. **728**: p. 1329-1337.

66. Arshad, A., et al., *Graphene nanoplatelets induced tailoring in photocatalytic activity and antibacterial characteristics of MgO/graphene nanoplatelets nanocomposites.* Journal of Applied Physics, 2017. **121**(2): p. 024901.
67. Chang, X., et al., *Graphene-tungsten oxide nanocomposites with highly enhanced gas-sensing performance.* Journal of Alloys and Compounds, 2017. **705**: p. 659-667.
68. Murugan, M., et al., *Facile hydrothermal preparation of niobium pentaoxide decorated reduced graphene oxide nanocomposites for supercapacitor applications.* Chemical Physics Letters, 2016. **650**: p. 35-40.
69. An, X., et al., *WO 3 nanorods/graphene nanocomposites for high-efficiency visible-light-driven photocatalysis and NO 2 gas sensing.* Journal of Materials Chemistry, 2012. **22**(17): p. 8525-8531.
70. Arshad, A., J. Iqbal, and Q. Mansoor, *NiO-nanoflakes grafted graphene: an excellent photocatalyst and a novel nanomaterial for achieving complete pathogen control.* Nanoscale, 2017. **9**(42): p. 16321-16328.
71. Comparelli, R., et al., *Photocatalytic degradation of azo dyes by organic-capped anatase TiO2 nanocrystals immobilized onto substrates.* Applied Catalysis B: Environmental, 2005. **55**(2): p. 81-91.
72. Rojas-Andrade, M.D., et al., *Antibacterial mechanisms of graphene-based composite nanomaterials.* Nanoscale, 2017. **9**(3): p. 994-1006.
73. Santhosh, C., et al., *Adsorption, photodegradation and antibacterial study of graphene–Fe 3 O 4 nanocomposite for multipurpose water purification application.* RSC Advances, 2014. **4**(54): p. 28300-28308.
74. Zou, F., et al., *Wrinkled surface-mediated antibacterial activity of graphene oxide nanosheets.* ACS applied materials & interfaces, 2017. **9**(2): p. 1343-1351.